THE INFLUENCE OF y^+ IN WALL FUNCTIONS APPLIED IN SHIP VISCOUS FLOWS

Internship report

Report No. : **Internship report**
Date : **February 2016**

MARIN
P.O. Box 28

6700 AA Wageningen
The Netherlands

T +31 317 49 39 11
F +31 317 49 32 45

E info@marin.nl
I www.marin.nl

THE INFLUENCE OF Y^+ IN WALL FUNCTIONS APPLIED IN SHIP VISCOUS FLOWS

Internship report

Reported by : S. ten Pas, BSc
Reviewed by : ir. J.C. Willemsen

Page intentionally left blank

PREFACE

This report is a result of my internship at MARIN (Maritime Research Institute Netherlands). The internship is a part of my study Mechanical Engineering, with specialisation Engineering Fluid Dynamics at the University of Twente supervised by prof.dr.ir. C.H. Venner (before prof.dr.ir. H.W.M. Hoeijmakers). During my 4-months long internship, there were a lot of people who helped me out with my questions and having a discussion with me about the results of my assignment. I would like to thank these people, where I want to thank a couple of them in particular.

At first I want to thank Chris Willemsen, my supervisor at MARIN, for giving me the opportunity to do an internship at MARIN and helping me with every question I had. I appreciate the fact that you put in a lot of effort to make my internship an interesting subject for both me as MARIN. For helping me with GridPro and answering my questions about the KVLCC2, I want to thank Filipe Pereira. Despite the fact that you were always very busy with your own projects, you always wanted to make time for me to help me out. I also want to thank Bart Schuiling, Jaap Windt and Serge Toxopeus for helping me with the Hexpress model of the KVLCC2 and Gerco Hagesteijn for being so kind to show me and the other students the test facilities at MARIN. At last I want to thank the students at MARIN, where I always had fun discussion with and learned a lot from about their different cultures.

Page intentionally left blank

SUMMARY

One approach to describe the solution of the shear-stress at a wall is the application of wall functions which determine the shear-stress at the wall from semi-empirical equations. The y^+ is the dimensionless quantity for the distance from the wall up to the centre of the first grid cell. In simulations without wall functions, this quantity is typically around 1, while wall functions allow us to take a y^+ higher than 1. The boundary layer can be divide in two region: the inner layer and the outer layer. The former also consist of three regions, which are from the wall up to the outer layer: the viscous sublayer ($y^+ < 5$), the buffer layer ($5 < y^+ < 30 - 50$) and the log-law region ($y^+ > 30 - 50$).

Grid are made with Gridpro (structured grids) and Hexpress (unstructured grids), where several configurations are chosen. For the Gridpro grids, 14 different y^+ values are chosen, with in every region of the inner layer some values. For most of the grids, also a grid refinement study is performed. For the Hexpress grids, 12 different y^+ values are chosen. Due to the lack of time, no grid refinement study is performed. CFD simulations are done with MARIN's in-house CFD solver ReFRESCO is used, which is an incompressible RANS solver.

From the simulation the friction resistance coefficient C_F and the pressure resistance coefficient C_P are evaluated. From the results followed that an y^+ between 50 and 100 is the most ideal case for both resistance coefficients. In the case only the friction resistance coefficient is considered, higher values in the log-law region can also be used to give satisfactory results.

Page intentionally left blank

CONTENTS

Page

NOMENCLATURE

Table 1: List of symbols

Symbol	Unit	Definition
ρ	[kg/m^3]	Density
t	[s]	Time
p	[Pa]	Pressure
μ	[Pa s]	Viscosity
ν_t	[m^{2}s^{-1}]	Eddy viscosity
x	[m]	x-coordinate
y	[m]	y-coordinate
z	[m]	z-coordinate
u	[m/s]	Velocity in x-direction
v	[m/s]	Velocity in y-direction
w	[m/s]	Velocity in z-direction
U_∞	[m/s]	Free-stream velocity
y^+	[-]	Dimensionless wall unit
y_m^+	[-]	Mean dimensionless wall unit
u^+	[-]	Dimensionless mean velocity
f	[kg m/s^2]	External body force
Re	[-]	Reynolds number
C_P	[-]	Pressure resistance coefficient
C_F	[-]	Friction resistance coefficient
F	[N]	Force
L_{pp}	[m]	Length between perpendiculars
τ_w	[Pa]	Wall shear stress
I	[-]	Turbulence intensity

Page intentionally left blank

LIST OF ABBREVIATIONS

Table 2: List of symbols

CFD	Computational Fluid Dynamics
DNS	Direct Numerical Simulation
KVLCC2	KRISO Very Large Crude Carrier
LES	Large Eddy Simulation
MARIN	Maritime Research Institute Netherlands
NS	No Slip condition
RANS	Reynolds-Averaged Navier-Stokes
ReFRESCO	REliable & Fast Rans Equations (solver for) Ships (and) Constructions Offshore
SST	Shear Stress Transport

Page intentionally left blank

REVIEW OF TABLES

Page intentionally left blank

REVIEW OF FIGURES

Page intentionally left blank

1 INTRODUCTION

Ships have always been an important way to transport people and goods over the water. Where ships in the beginning were powered by the wind, nowadays most of them are driven by a propeller. People try to lower the fuel costs of these ships as much as possible. An important factor in the efficiency of ships is therefore the friction force a ship experiences while sailing. One tries to design a ship in such a way that these forces are as low as possible. The friction forces can be determined with experiments done in experimental facilities such as wind tunnels and towing tanks. But making and testing full scale models in those facilities is hard and expensive. Another way to determine these forces is to numerically simulate the viscous flows. Due to the computational effort needed, this was hard to achieve years ago. But nowadays, with the increasing development of computers, the subsequent increase in memory capacity and calculation speed allows for the numerical study of fluid dynamics problems, such as determining the friction forces. The method of studying fluid flow related problems with computer based simulations is called Computational Fluid Dynamics (CFD).

Most of the flows we experience in nature are turbulent flows and many of these exhibit high Reynolds numbers, such as in this study. An essential feature of turbulent flows is that the fluid velocity field varies significantly and irregularly in both position and time. There are several methods which can be used to numerically solve turbulent flows. Three common approaches are direct numerical simulation (DNS), large-eddy simulation (LES) and the Reynolds-Averaged Navier-Stokes equations (RANS), where RANS will be discussed in this study.

On the wall of a ship the no slip condition cause large pressure gradients in the solution. To directly describe these large gradients a narrow grid close to the wall is required, which results in a large grid size and therefore high computation time. Another approach to describe the solution of the shear-stress at a wall is the application of wall functions which determine the shear-stress at the wall from semi-empirical equations applicable up to the outer edge of the so-called "wall layer/log layer". Applying this method will reduce the number of cells and therefore lower the computation time. The drawback is that it is less accurate than the direct application of the no slip condition.

The purpose of this study is to determine the effect of the dimensionless wall unit y^+ with the use of wall functions on the resistance and flow for a KVLCC2 tanker. The different values for y^+ are taken such that they are in different regions of the boundary layer, for example the buffer layer and the log-law region. The test case selected is the KVLCC2 tanker, one of the ship hulls of the Workshops on Numerical Ship Hydrodynamics [3, 4]. The results will be compared with the results from the direct application of the no-slip condition, i.e. simulations without the use of wall functions. The calculations will be done with ReFRESCO, which is a CFD-solver for the RANS equations developed by MARIN.

Chapter 2 give some more information about the solver and the theory behind wall functions. Chapter 3 give information about the calculation process and grids used and chapter 4 contains the results of the simulations. The conclusions and recommendations are stated in chapter 5.

2 THEORY

2.1 Navier-Stokes equations

The Navier-Stokes equations are the fundamental equations in physics and are based on the conservation of mass, the conservation of momentum (Newton's second law) and the conservation of energy (the first law of thermodynamics). The law of conservation of mass states that for any system closed to all transfers of matter and energy, the mass of the system must remain constant over time. This results in the continuity equation in differential form:

$$\frac{\partial \rho}{\partial t} + \vec{\nabla} \cdot (\rho \vec{u}) = 0 \tag{1}$$

Where ρ is the density and $\vec{u}$ the velocity of the fluid. The momentum equation follows from Newton's second law ($\vec{F} = \frac{\mathrm{d}}{\mathrm{d}t}(m\vec{u})$ and describes the conservation of momentum. In partial differential form it is written as:

$$\frac{\partial}{\partial t}(\rho \vec{u}) + \vec{\nabla} \cdot (\rho \vec{u}\vec{u}) = \rho \vec{f} - \vec{\nabla} p + \vec{\nabla} \cdot \overline{\overline{\tau}} \tag{2}$$

Where $\vec{f}$ are the external body forces, p is the pressure of the fluid and $\overline{\overline{\tau}}$ is the viscous stress tensor, which is given (in Cartesian coordinates) as:

$$\overline{\overline{\tau}} = \begin{pmatrix} \tau_{xx} & \tau_{yx} & \tau_{zx} \\ \tau_{xy} & \tau_{yy} & \tau_{zy} \\ \tau_{xz} & \tau_{yz} & \tau_{zz} \end{pmatrix} \tag{3}$$

The exact derivation of these equations and the equation for the conservation of energy can be found in Peric [5].

2.2 Turbulent flows

Flows at high Reynolds number are turbulent flows, with only portions of the flow being laminar. A laminar flow is a regular flow, often constant in time, while turbulent flow is mostly irregular, 3D and unsteady. In turbulent flow, unsteady vortices appear on many scales and interact with each other. Figure 1 shows a simple illustration of laminar and turbulent flows.

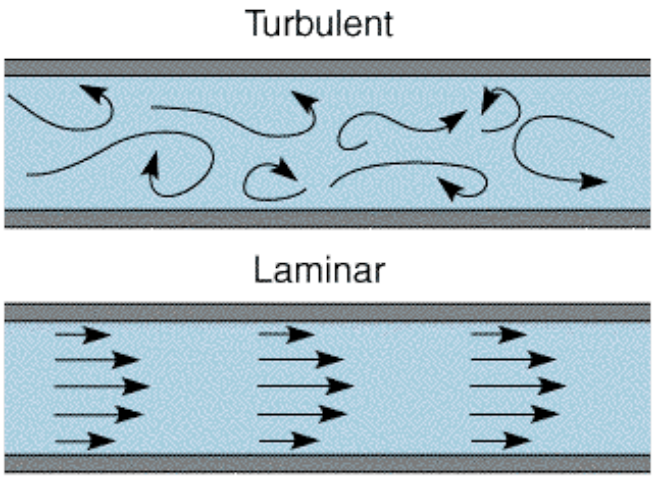

Figure 1: Difference between laminar and turbulent flow

An essential feature of turbulent flows is that the fluid velocity field varies significantly and irregularly in both position and time. There are several methods which can be used to numerical solve turbulent flows. Three common approaches are direct numerical simulation (DNS), large-eddy simulation (LES) and the Reynolds-Averaged Navier-Stokes equations (RANS). Direct numerical simulation resolves the entire range of turbulent length scales, which marginalizes the effect of models, but is therefore extremely expensive. The computational cost is proportional to Re^3 [6]. With large eddy simulation the smallest scales are eliminated by low-pass filtering, which allows the largest and most important scales of the turbulence to be resolved, while reducing the computational cost incurred by the smallest scales [6]. The Reynolds-Averaged Navier-Stokes equations are time-averaged equations of motion for fluid flows. For most engineering problems, this method provides a good accuracy with low computation times. In this study, only the RANS equations will be used.

2.2.1 Reynolds-Averaged Navier-Stokes equations

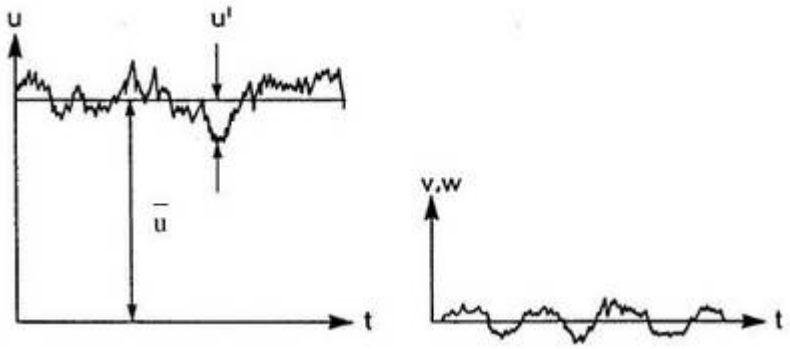

Figure 2: Turbulent velocity fluctuation in pipe flow as a function of time [1]

The idea behind the Reynolds-Averaged Navier-Stokes equations is Reynolds decomposition, whereby an instantaneous quantity is decomposed into its time-averaged and fluctuating quantities (shown graphically in figure 2), an idea first proposed by Osborne Reynolds [7]. It states that in a statistically steady flow, every variable ϕ can be written as the sum of a time-averaged part $\overline{\phi}(\vec{x})$ and a fluctuation of that value $\phi'(\vec{x},t)$:

$$\phi(\vec{x},t) = \overline{\phi}(\vec{x}) + \phi'(\vec{x},t) \tag{4}$$

Where the time-averaged value $\overline{\phi}(\vec{x})$ is defined as:

$$\overline{\phi}(\vec{x}) = \lim_{T\to\infty} \frac{1}{T} \int_0^T \phi(\vec{x},t)\mathrm{d}t \qquad \text{and} \qquad \overline{\phi'}(\vec{x},t) = \lim_{T\to\infty} \frac{1}{T} \int_0^T \phi'(\vec{x},t)\mathrm{d}t = 0 \tag{5}$$

From equation (4) and equation (5) follows:

$$\overline{\overline{\phi}} = \overline{\phi}, \quad \overline{\phi'} = 0, \quad \overline{\phi + \sigma} = \overline{\phi} + \overline{\sigma}, \quad \overline{\overline{\phi} \cdot \sigma} = \overline{\phi} \cdot \overline{\sigma} \tag{6}$$

Where σ is another variable in the flow with $\overline{\sigma}(\vec{x})$ its time averaged value. For incompressible Newtonian fluid, the Navier-Stokes equations of motion, expressed in tensor notation, are:

$$\frac{\partial u_i}{\partial x_i} = 0 \tag{7a}$$

$$\rho\frac{\partial u_i}{\partial t} + \rho u_j\frac{\partial u_i}{\partial x_j} = \rho f_i - \frac{\partial p}{\partial x_i} + \mu\frac{\partial^2 u_i}{\partial x_j \partial x_j} \tag{7b}$$

Where f_i is a vector representing external forces. For the continuity equation, applying the Reynolds decomposition and taking the average will lead to:

$$\overline{\frac{\partial(\overline{u_i} + u_i')}{\partial x_i}} = \overline{\frac{\partial \overline{u_i}}{\partial x_i}} + \overline{\frac{\partial u_i'}{\partial x_i}} = 0 \tag{8}$$

Which we can rewrite with the rules in equation (6) to the time averaged continuity equation:

$$\frac{\partial \overline{u_i}}{\partial x_i} = 0 \tag{9}$$

For the momentum equation, applying the Reynolds decomposition and taking the average will lead to:

$$\overline{\rho\frac{\partial(\overline{u_i} + u_i')}{\partial t} + \rho(\overline{u_j} + u_j')\frac{\partial(\overline{u_i} + u_i')}{\partial x_j}} = \overline{\rho f_i - \frac{\partial(\overline{p} + p')}{\partial x_i} + \mu\frac{\partial^2(\overline{u_i} + u_i')}{\partial x_j \partial x_j}} \tag{10}$$

Which we can rewrite with the rules in equation (6) to the time averaged momentum equation:

$$\rho\frac{\mathrm{D}\overline{u_i}}{\mathrm{D}t} + \rho\overline{u_j'\frac{\partial u_i'}{\partial x_j}} = \overline{\rho f_i} - \frac{\partial \overline{p}}{\partial x_i} + \mu\frac{\partial^2 \overline{u_i}}{\partial x_j \partial x_j} \tag{11}$$

With the help of equation (9) we can rewrite this equation to:

$$\rho\frac{\mathrm{D}\overline{u_i}}{\mathrm{D}t} = \overline{\rho f_i} - \frac{\partial \overline{p}}{\partial x_i} + \frac{\partial}{\partial x_j}\left(\mu\frac{\partial \overline{u_i}}{\partial x_j} - \rho\overline{u_i' u_j'}\right) \tag{12}$$

Where $R_{ij} = -\rho\overline{u_i' u_j'}$ is commonly known as the Reynolds stresses. It is a symmetrical tensor, which introduces 6 new unknowns for a tridimensional flow. This leads to a total of 10 unknowns and 4 equations. Therefore, the system needs additional equations in order to be closed. This is known as the turbulence closure problem of the RANS equations [8].

2.2.2 Eddy viscosity

Joseph Boussinesq introduced the eddy-viscosity model for the Reynolds stress [9] . He proposed relating the turbulence stresses to the mean flow to close the system of equations and assumed that the Reynolds stresses are proportional to the mean velocity gradients:

$$-\rho\overline{u_i' u_j'} = \mu_t\left(\frac{\partial \overline{u_i}}{\partial x_j} + \frac{\partial \overline{u_j}}{\partial x_j}\right) - \frac{2}{3}\rho\delta_{ij}K \tag{13}$$

Which can be written in shorthand as

$$-\rho\overline{u_i' u_j'} = 2\mu_t S_{ij} - \frac{2}{3}\rho\delta_{ij}K. \tag{14}$$

The K term is the so-called turbulent kinetic energy given by $K = \frac{1}{2}\overline{u_i' u_i'}$ and δ_{ij} is the Kronecker symbol. The turbulence can be then characterized by two parameters, or two scales, the turbulence velocity scale v and the turbulence length scale l, i.e. $\mu_t \sim \rho v l$. Some turbulence models work directly with the kinematic viscosity $\nu_t = \frac{\mu_t}{\rho}$.

2.2.3 Turbulence transport models

A turbulence model is a set of equations, additional to the RANS equations, purporting to express relations between terms appearing in those equations. The starting point of all transport models is equation (12) and the problem of 'closure' reduces to the modeling of the Reynolds stresses $R_{ij} = -\rho\overline{u_i' u_j'}$, in terms of mean-flow quantities.

The traditional linear-eddy-viscosity RANS models may be divided into the following four main categories [10]: algebraic (zero-equation) models, half equation models, one-equation models and two-equation models. In this study, only the two-equation SST $k-\omega$ model is used.

Two equation-models are models in which model transport equations are solved for two turbulence quantities. These models are therefore complete, i.e. can be used to predict properties of a given turbulent flow with no prior knowledge of the turbulent structure.

- $k-\varepsilon$ Model
  The 2-equation $k-\varepsilon$ model [11] is one of the most used and referred turbulence model available in the literature. The first transported variable determines the energy in the turbulence and is called turbulent kinetic energy k. The second transported variable is the turbulent dissipation ε which determines the rate of dissipation of the turbulent kinetic energy.

- $k-\omega$ Model
  The $k-\omega$ model by Wilcox [12] is based on 2 transport equations, one for the turbulence kinetic energy k and the other for ω, which represents a characteristic frequency of the turbulence. Its simple formulation for the sub-viscous layer and the decoupling between the k and ω render numerically robust model.

- $k-\omega$ SST Menter Model (1994)
  It is well known [13] that models based on the ε-equation lead to an over prediction of the turbulent length scale in flows with adverse pressure gradients, resulting in high-wall shear stress and high transfer rates. The ω equation in contrast, has significant advantages near the surface and accurately predicts the turbulent length scale in adverse pressure gradient flows, leading to improved wall shear stress. It was pointed out by Menter [14] that the main deficiency of the standard $k-\omega$ model is the strong sensitivity of the solution to free stream values for ω outside the boundary layer. In order to avoid this problem, a combination of the $k-\omega$ near the wall and the $k-\varepsilon$ model away from the wall has been proposed, leading to the SST (Shear-Stress-Transport) model [15]. This model combines the benefits from both the $k-\omega$ model and the $k-\varepsilon$ model.

- $k-\omega$ SST Menter Model (2003)
  This model slightly differs from the model proposed in the SST Menter Model (1994). Robustness optimisation have brought the model to the same level of convergence as the standard $k-\varepsilon$ model with wall function and an improved near-wall formulation has reduced the near wall grid resolution requirements [16].

2.3 Wall functions

As mentioned before, the near-wall flow fields requires special treatment. In RANS there are two main approaches for the determination of the shear-stress at a wall: direct application of the no-slip condition and wall functions which determine the shear-stress at the wall from semi-empirical equations. The y^+ is the dimensionless quantity for the distance from the wall up to the centre of the first grid cell. The y^+ of the first method is typically around 1, while wall functions allow us to take a y^+ higher than 1. This results in a lower amount of grid cells and therefore lower computation times.

The idea behind the 'wall-function' approach [17] is to apply boundary conditions (based on log-law relations) some distance away from the wall, so that the turbulence-model equations are not solved close to the wall (i.e., between the wall and the location at which boundary conditions are applied) [6]. There are some drawbacks for using wall function:

- The use of wall functions assumes the flow to be fully-turbulent.
- The "log-law" is invalid in strongly three-dimensional flows, in particular in regions of separated flow

Since the flow in this study is mostly fully-turbulent and not strongly three-dimensional, it allows us to make use of wall functions.

2.3.1 The law of the wall

It is evident that, close to the wall, the viscosity ν and the wall shear stress τ_w are important parameters. From these quantities (and ρ) we define viscous scales that are the appropriate velocity scales and length scales in the near-wall-region. These are the friction velocity:

$$u_\tau \equiv \sqrt{\frac{\tau_w}{\rho}} \tag{15}$$

And the viscous length scale

$$\delta_\nu \equiv \mu\sqrt{\frac{\rho}{\tau_w}} = \frac{\mu}{u_\tau} \tag{16}$$

The distance from the wall measured in viscous length - or wall units - is denoted by:

$$y^+ \equiv \frac{y}{\delta_\nu} = \frac{u_\tau y}{\nu} \tag{17}$$

Prandtl [18] postulated that, at high Reynolds number, close to the wall ($\frac{y}{\delta} \ll 1$) there is an inner layer in which the mean velocity profile is determined by the viscous scales, independent of δ and the reference velocity U_0:

$$\frac{\mathrm{d}u^+}{\mathrm{d}y^+} = \frac{1}{y^+}\Phi_I(y^+) \tag{18}$$

With

$$\Phi_I(y^+) = \lim_{\frac{y}{\delta}\to 0} \Phi\left(\frac{y}{\delta_\nu}, \frac{y}{\delta}\right) \tag{19}$$

Where Φ is a universal non-dimensional function. The integral of equation (18) is the law of the wall:

$$u^+ = f_w(y^+) \tag{20}$$

Where

$$f_w(y^+) = \int_0^{y^+} \frac{1}{y'} \Phi_I(y') \mathrm{d}y' \tag{21}$$

The important point is the fact that (according to Prandtl's hypothesis) u^+ depends solely on y^+ for $\frac{y}{\delta} \ll 1$. For Reynolds numbers not too close to transition, there is abundant experimental verification that the function f_w is universal.

2.3.2 The inner layer

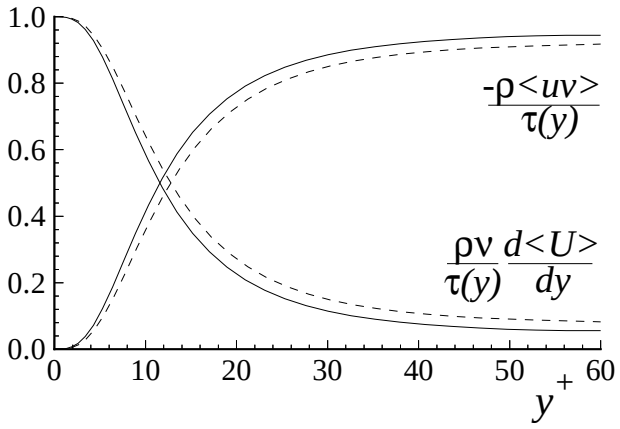

Figure 3: Profiles of the fractional contributions of the viscous and Reynolds stresses to the total stress. DNS data of [2]: dashed lines, $Re = 5600$; solid lines, $Re = 13750$.

Figure 3 shows us the fractional contributions of the viscous and Reynolds stresses to the total stress. We can divide the inner layer ($\frac{y}{\delta} < 0.1$) into three subregions: The viscous sublayer, where the Reynolds stresses are negligible; the log-layer, where the viscous stresses are negligible; and the buffer layer, where none of them are negligible. The viscous sublayer is valid from the wall up to approximately $y^+ = 5$. The law-of-the-wall for this layer is expressed in dimensionless form in the following way:

$$u^+ = y^+ \tag{22}$$

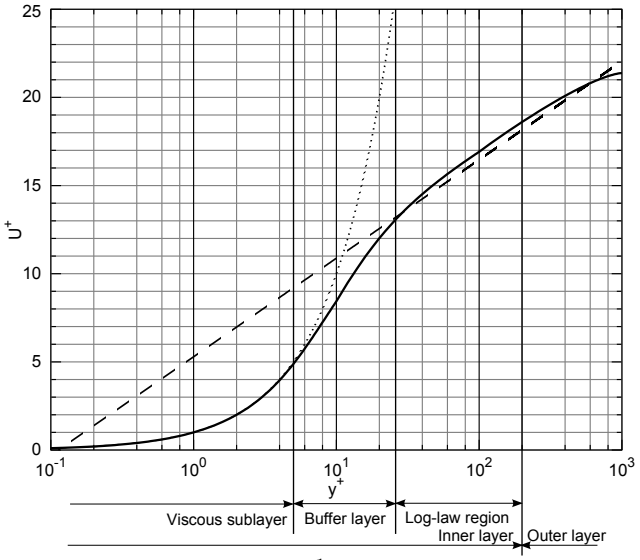

Figure 4: Dotted line: $u^+ = y^+$, striped line: $u^+ = \frac{1}{\kappa} \ln y^+ + B$, solid line: experimental data

The log-layer is valid from $y+ = 30 - 50$ to the outer edge of the law-of-the-wall region, which depends on the Reynolds number. The law-of-the-wall for this layer is expressed in dimensionless form in the following way:

$$u^+ = \frac{1}{\kappa} \ln y^+ + B \tag{23}$$

Where B is a constant and κ is the von Kármán constant. This is the logarithmic law of the wall [19]. In the literature, there is some variation in the values ascribed to the log-law constants, but generally they are within 5% of $\kappa = 0.41$ and $B = 5.2$. Finally, the buffer-layer is located on the region $5 < y^+ < 30 - 50$. Neither of the law holds in this region. Figure 4 gives an illustration of the derived expressions.

2.3.3 Automatic wall function

Wall functions are not always desirable, as they neglect the influence of the viscous sublayer. Especially for flows at low device Reynolds numbers, the omission of the sublayer can have a significant effect on the solution. Menter and Esch [20] proposed the automatic wall function. The idea behind the automatic near-wall treatment is that the model shifts gradually between a viscous sublayer formulation and wall functions, based on the grid density. A blending function depending on y^+ can therefore be defined. The ω-equation is well suited for this task, as it provides analytical solutions, both for the viscous sublayer and the log-layer.

2.4 Flow Solver ReFRESCO

ReFRESCO is an acronym for REliable & Fast Rans Equations (solver for) Ships (and) Constructions Offshore and is currently being developed, verified and validated at MARIN (in the Netherlands) [21, 22, 23, 24, 25, 26, 27] in collaboration with several other institutes and universities. ReFRESCO is a viscous-flow CFD code that solves multiphase (unsteady) incompressible flows using the Navier-Stokes equations, complemented with turbulence models, cavitation models and volume-fraction transport equations for different phases [28]. The equations are discretized using a finite-volume approach with cell-centered collocated variables,

in strong-conservation form, and a pressure-correction equation based on the SIMPLE algorithm is used to ensure mass conservation [29].

The equations are supplemented by a turbulence model, which is in this case the two-equations SST $k-\omega$ model from 2003 (SST-2003) [16]. The wall function used is the Automatic Wall function proposed by Menter [30].

Hence the governing equations are coupled, ReFRESCO solves them in a segregated way. Also, the momentum equations are linearized using a simple Picard-type of linearization [5]. By iteration the coupling and the non-linear character of the equation is restored. A schematical overview can be found in Appendix II.

2.5 Numerical uncertainty

In order to determine the quality of the computational results, verification and validation studies are required. Verification is a purely mathematical exercise that intends to show that we are "solving the equations right", whereas validation is a science/engineering activity that intends to show that we are "solving the right equations" [31]. This means that verification deals with numerical errors/uncertainties whereas validation is concerned with modelling errors/uncertainties. Verification consists of two parts [31]:

1. Code verficication, intending to demonstrate by error evaluation the correctness of the code that contains the algorithm to solve a given mathematical model
2. Solution verification, attempting to estimate the error/uncertainty of a given numerical solution, for which, in general, the exact solution is unknown.

It is assumed that the code solves the equations of the model correctly and therefore only solution verification will be part of this study. Furthermore it is assumed that the round-off error is small compared to the iterative error and the discretization error and that the iterative error is more than two to three order of magnitude smaller than the discretization error, so that it will not disturb the estimation of the numerical error. The method proposed by Eça [32] will be used. For this method it is required to have the solution for at least four grids ($n_g \geq 4$).

2.5.1 Error estimation

The estimation of the discretization error will be done with the truncated power series expansion:

$$\epsilon_\phi \simeq \delta_{RE} = \phi_i - \phi_0 = \alpha h_i^p \tag{24}$$

Where ϕ_i stands for any integral or other functional of a local flow quantity, ϕ_0 is the estimate of the exact solution, h_i is the typical cell size, p is the order of grid convergence and α is a constant which has to be determined. When the estimation of equation (24) is impossible or not reliable, i.e. the observed order of grid convergence is either too small or too large, three other error estimators are added:

$$\epsilon_\phi \simeq \delta_1 = \phi_i - \phi_0 = \alpha h_i \tag{25a}$$

$$\epsilon_\phi \simeq \delta_2 = \phi_i - \phi_0 = \alpha h_i^2 \tag{25b}$$

$$\epsilon_\phi \simeq \delta_{12} = \phi_i - \phi_0 = \alpha_1 h_i + \alpha_2 h_i^p \tag{25c}$$

It is possible to do the error estimation in the least-square sense. In the case four or more grids are used, one may wish to give more value to the finer than the coarser grid solutions, which can be done with a weighted approach of the least-square sense. Both the weighted and non-weighted least-square functions with their standard deviations are given in Appendix .

At first, the order of grid convergence will be determined with the error estimator of equation (24) for both the weighted and non-weighted approach. If both fits exhibit $0.5 \leq p \leq 2$, the value of δ_{RE} selected corresponds to the fit with the smallest standard deviation. If only one of the fit exhibit $0.5 \leq p \leq 2$, that particular fit is selected. If both fits do not exhibit $0.5 \leq p \leq 2$, the value of p selected corresponds to the fit with the smallest standard deviation. Now the following procedure is followed:

- $p > 2$
  In this case, δ_1 and δ_2 are solved in the least-square sense with and without weights and ϵ_ϕ is obtained from the fit that exhibits the smallest standard deviation.
- $p < 0.5$
  In this case, δ_1, δ_2 and also δ_{12} are solved in the least-square sense with and without weights and ϵ_ϕ is obtained from the fit that exhibits the smallest standard deviation.

2.5.2 Uncertainty estimation

The aim of solution verification is to estimate the numerical uncertainty, U_ϕ, of a solution, ϕ_i for which we do not know the exact solution, ϕ_{exact}. The goal is to define an interval that contains the exact solution with a 95% confidence [33]:

$$\phi_i - U_\phi \leq \phi_{exact} \leq \phi_i + U_\phi \tag{26}$$

The quality of the fit can be determined with a data range parameter Δ_ϕ:

$$\Delta_\phi = \frac{(\phi_i)_{\text{max}}(\phi_i)_{\text{min}}}{n_g - 1} \tag{27}$$

Where n_g is the amount of data points. The error estimation is considered reliable if the solution is monotonically convergent with $0.5 \leq p \leq 2.1$ and if the standard deviation $\sigma < \Delta_\phi$. In this case, following the Grid Convergence Index (GCI) procedure [31, 34], this lead to a safety factor of $F_s = 1.25$. In any other cases, $F_s = 3$. The uncertainty estimation can now be determined:

- For $\sigma < \Delta_\phi$

$$U_\phi(\phi_i) = F_s \epsilon_\phi(\phi_i) + \sigma + |\phi_i - \phi_{\text{fit}}| \tag{28}$$

- For $\sigma \geq \Delta_\phi$

$$U_\phi(\phi_i) = 3\frac{\sigma}{\Delta_\phi}(\epsilon_\phi(\phi_i) + \sigma + |\phi_i - \phi_{\text{fit}}|) \tag{29}$$

3 CALCULATION DETAILS

The CFD simulations are done for different grids and different values of y^+. This chapter first describes the calculation parameters used for the incoming flow and describes the geometry of the ship used for the simulation. After that, the grid generation procedure is shortly described for both grids made with GridPro and Hexpress. It also shows some illustration of some of the grids to give a feeling of how the grids are constructed.

3.1 Ship Geometry, Flow Conditions and Computational Domain

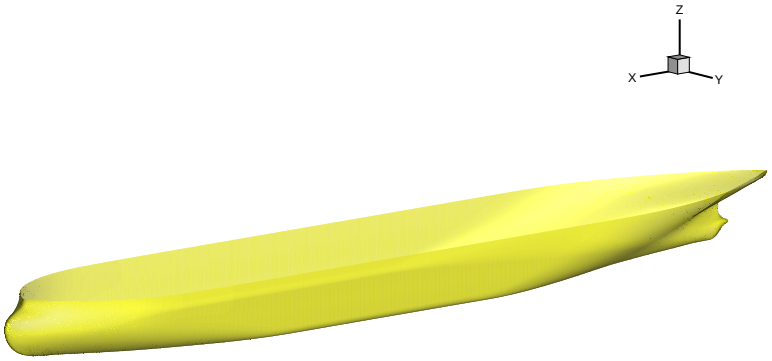

Figure 5: KVLCC2 tanker

The test case selected is the KVLCC2 tanker (figure 5), one of the ship hulls of the Workshops on Numerical Ship Hydrodynamics [3, 4]. The full scale Reynolds number is considered. Based on the undisturbed flow velocity $U_\infty = 7.5$ m/s and length between perpendiculars $L_{pp} = 320.0$ m, this leads to a Reynolds number of $Re = 2.03 \times 10^9$, which is the Reynolds number used in previous studies on the KVLCC2 [35].

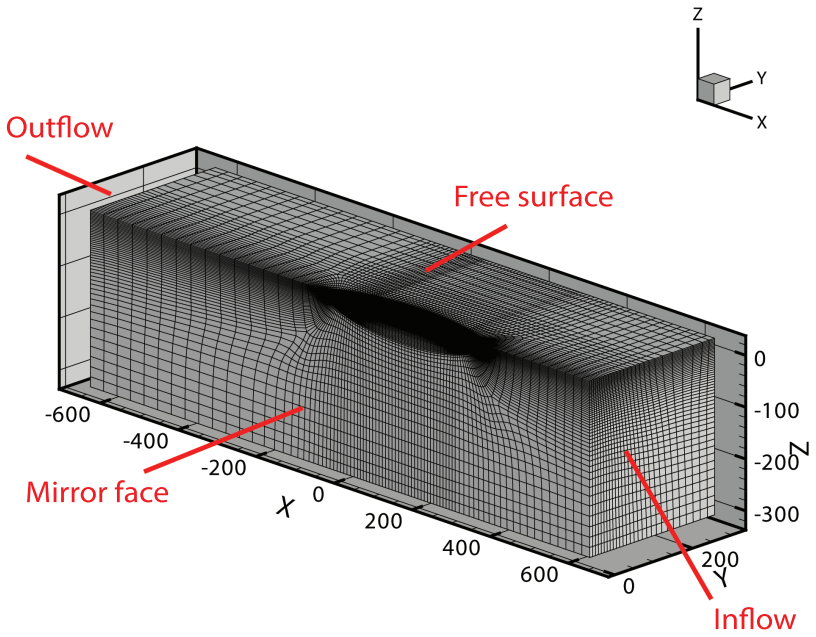

Figure 6: Grid of the computational domain

The computational domain has a rectangular shape and is initially generated with GridPro and later Hexpress. The boundaries of the domain are $x = -640$ (inlet plane) and $x = 640$ (outlet plane), the planes $y = 0$ (symmetry plane of the ship) and $y = 320$ (pressure plane), $z = 20.8$ (still water plane) and $z = -320$ (slip wall plane) and the surface of the ship. More flow conditions can be found in table 3. A graphical illustration of the computational domain can be found in figure 6.

All the calculations presented in this study are performed with ReFRESCO. In this study, a solution is declared converged when the L-infinity norm L_∞ of all the residuals are less than 10^{-5}. More calculation details can be found in table 3.

Description	**Symbol**	**Magnitude**	**Unit**
Reynolds number	Re	2.03×10^9	-
Reference velocity	V_{ref}	7.5495	m/s
Reference length	L_{ref} or L_{pp}	320	m
Density	ρ	1025.99	kg/m^3
Dynamic viscosity	μ	1.221×10^{-3}	Pa s
Turbulence intensity (inlet)	$I = \frac{u'}{U_\infty}$	0.1	-
Ratio $\frac{\mu_t}{\mu}$ (inlet)		10.0	-

Table 3: Flow conditions

3.2 GridPro grids

With GridPro it is possible to generate structured grids. Due to the fact that the grid can be coarsened or refined in a structural way, this type of grids can be very useful for grid refinement studies. To generate grids with different resolution and different y^+ values, an initial grid is made at first. From this grid, a first cell distance and a cell growth ratio can be defined, so that a new grid can be generated. This grid can then be coarsened to get grids with less cells, which can be useful for the grid refinement studies.

3.2.1 Wall distance

To determine the wall distance related to a specific y^+, the friction coefficient has to be known. The skin friction coefficient is defined as:

$$C_f \equiv \frac{\tau_w}{\frac{1}{2}\rho U_\infty^2} \tag{30}$$

Where τ_w is the local wall shear stress, ρ is the fluid density and U_∞^2 is the free-stream velocity. We can estimate this friction coefficient as a function of the Reynolds number with the Schultz-Grunow relation [36]:

$$C_f = 0.370 \left(\log Re_x\right)^{-2.584} \tag{31}$$

We can rewrite equation 30 to get the local wall shear stress:

$$\tau_w = C_f \frac{1}{2}\rho U_\infty^2 \tag{32}$$

Combining equations (15) and (17) and rewriting yields:

$$y = \frac{y^+ \mu}{\rho \sqrt{\frac{\tau_w}{\rho}}} \tag{33}$$

The first cell distance used by Gridpro and Hexpress is now equal to two times the y.

3.2.2 Grid generation

To determine the influence of y^+, a wide range of y^+ values are selected. These values are selected so that in each region (viscous sublayer, buffer layer and log-law region) there are sufficient data points available to give a good impression of what happens in each region. This leads to 5 points in the viscous sublayer (0.5, 1.5, 2.5, 3.5 and 5), 4 points in the bufferlayer (7.5, 12.5, 22.5 and 37.5) and 5 points in the log-law region (50, 112.5, 250, 500, 1500). For every y^+ value there are 7 different grids generated to perform a grid refinement study, except for $y^+ = 0.5, 1.5$ and 3.5, where only the finest grid is generated.

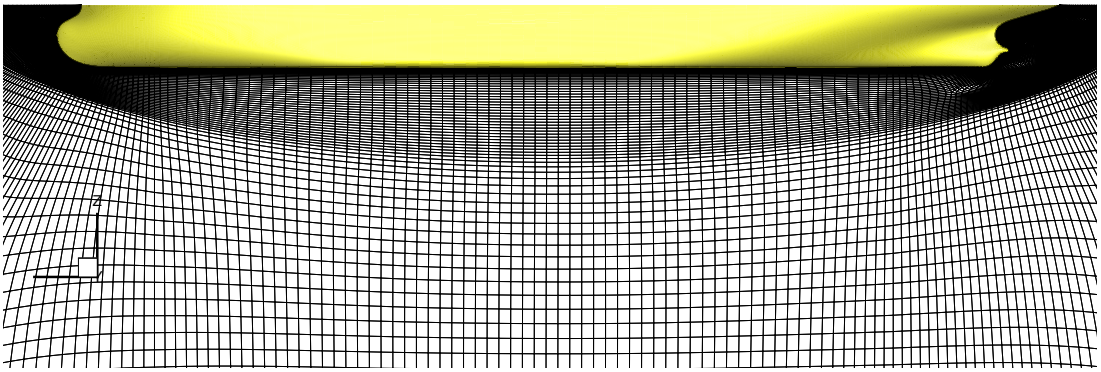

Figure 7: Grid G5 (with coarsening ratio 0.5000) for $y^+ = 250$

Figure 7 shows the grid G5 (corresponding to coarsening ratio 0.5000) for $y^+ = 250$. It can be seen that the grid is finer at the grid and the stern. Figure 8 shows a closer look at the bow and the stern.

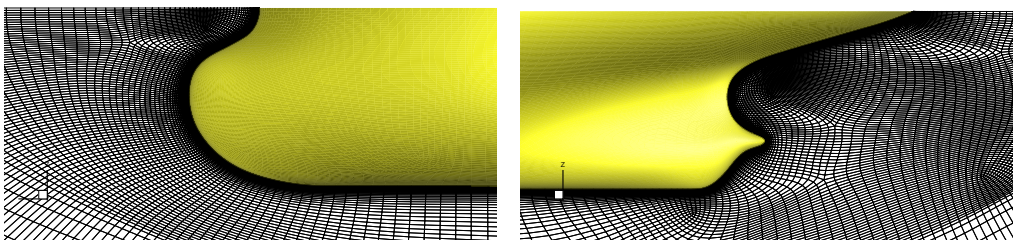

(a) Grid at the bow of the ship *(b) Grid at the stern of the ship*

Figure 8: Parts of the grid G5 (with coarsening ratio 0.5000) for $y^+ = 250$

More details about the grids (e.g. the amount of cells for every grid) can be found in Appendix IV.

3.3 Hexpress grids

Hexpress generates unstructured grids, which are easier to generate for complex, realistic geometries. Another advantage is the ability to dynamically adapt the grid to local features of interest, for example the bow of the KVLCC2. A disadvantage of unstructured grids is that the solution will converge slower in comparison with structured grids.

3.3.1 Different model

The geometry used for the grids made in Gridpro could not be used in Hexpress due to compatibility errors in the input files. This means that the models differs a little from eachother. Figure 9a shows the differences at the bow and figure 9b shows the difference at the stern, where the red lines is the model used with Hexpress and the black lines is the model used with Gridpro. The differences are small and can not easily be seen, but they can cause small differences in the solution.

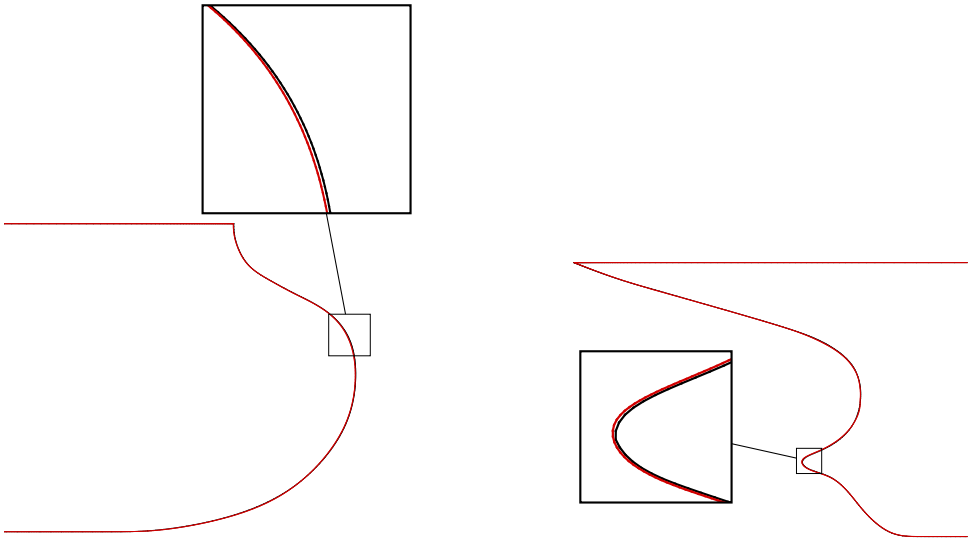

(a) Difference at the bow *(b) Difference at the stern*

Figure 9: Difference between the Gridpro model (black lines) and Hexpress model (red lines)

3.3.2 Grid generation

For Hexpress two different kind of grids are generated: one grid with 0.944 million grid cells before applying the viscous layer (after this called 944k) and one grid with 3.511 million grid cells before applying the viscous layer (after this called 3511k). For the former, only grids with a y^+ in the log-law region are generated and for the latter grids with an y^+ in the whole range of the inner layer is generated (i.e. viscous sublayer, buffer layer and log-law region).

Figure 10 shows the grid for type 3511k with an $y^+ = 250$. A better look at the bow and the stern can be seen in figure 11, where clearly the unstructured character of the grid comes forward.

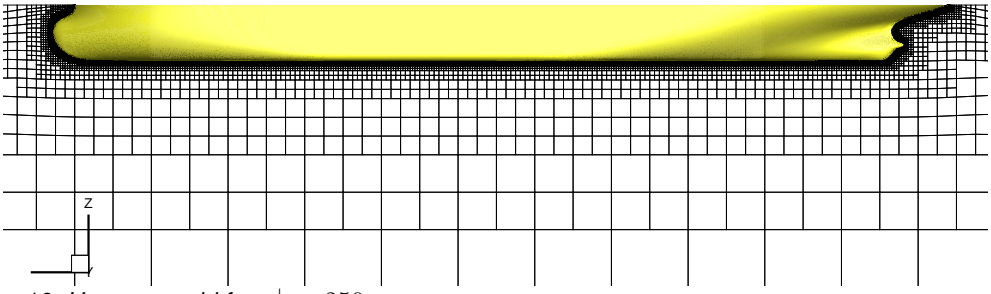

Figure 10: Hexpress grid for $y^+ = 250$

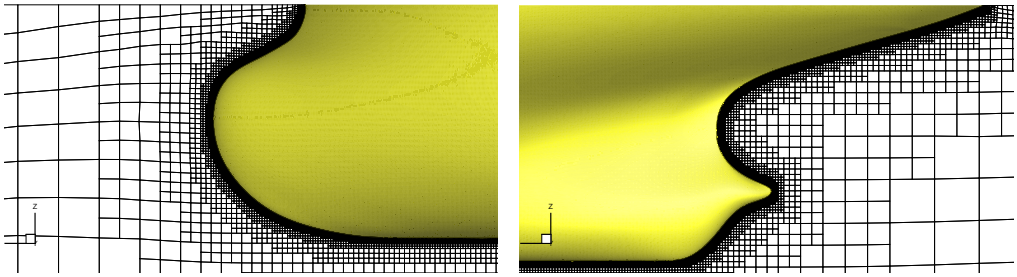

(a) The Hexpress grid zoomed in at the bow *(b) The Hexpress grid zoomed in at the stern*

Figure 11: Hexpress grid for $y^+ = 250$

More details about the grids (e.g. the amount of cells for every grid) can be found in Appendix IV.

4 RESULTS

The chapter contains the results of the simulation done in this study. First the selected flow quantities which are used to compare the different results are described. After that the results of the simulations done with the GridPro grids are presented. This is done by first presenting the results for the grid study, to determine the grid quality. It will be followed by the results for the friction resistance coefficient and the pressure resistance coefficient. For the Hexpress grids, no grid study is done. This means only the simulation results of the friction resistance coefficient and the pressure resistance coefficient and compared to the results gained with the Gridpro grids.

4.1 Selected Flow Quantities

In order to assess the impact of wall function boundary conditions on the calculation of viscous flows with the RANS equations, the friction C_f and pressure C_p resistance coefficients are selected. These are defined as:

$$C_F = \frac{F_{f,x}}{\frac{1}{2}\rho U_\infty^2 S_w} \tag{34a}$$

$$C_P = \frac{F_{p,x}}{\frac{1}{2}\rho U_\infty^2 S_w} \tag{34b}$$

Where $F_{f,x}$ is the friction force in x-direction, $F_{p,x}$ is the pressure force in x-direction and S_w is the ship wetted surface (which is extracted from Tecplot). Because the y^+ is not the same at every point on the surface, a quantity has to be calculated which describes the mean value of y^+. This value y_m^+ is defined as:

$$y_m^+ = \frac{\int_{S_w} y^+ \mathrm{d}S}{S_w} \tag{35}$$

4.2 GridPro results

Figure 12 shows the velocity in x-direction around the ships surface. It can be seen that just before the bow and the stern of the ship, the velocity gradient is relatively bigger than at the bow or stern itself.

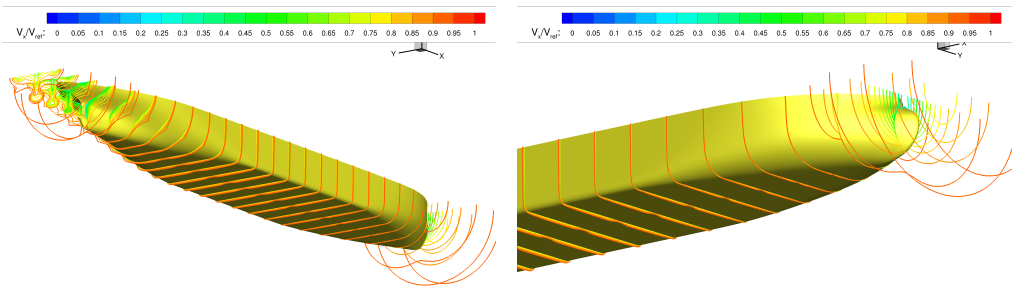

(a) Velocity in x-direction around the hull of the ship

(b) Velocity in x-direction around the bow of the ship

Figure 12: Simulation results of the velocity in x-direction for $y_m^+ = 116.8$ and grid size G1

Figure 13 shows the friction resistant coefficient on the ships surface. It can be seen that the highest friction force will be experienced at the bottom of the hull just after the bow and at the bottom of the hull just before the stern of the ship. This are the regions where the velocity around the ships surface accelerate (just after the bow of the ship) or decelerate (just before the stern of the ship), as can be seen in figure 12.

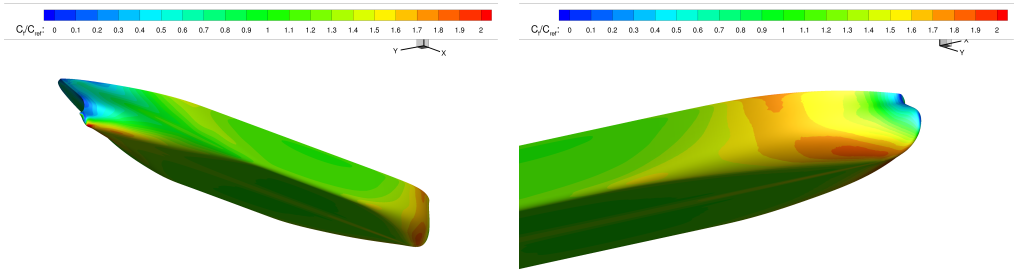

(a) Friction force at the hull of the ship *(b) Friction force at the bow of the ship*

Figure 13: Simulation results of the friction coefficient for $y_m^+ = 116.8$ and grid size G1

Figure 14 shows the pressure resistance coefficient on the ships surface. It can be seen that the highest forces will experienced at the bow of the ship (figure 14b), where the flow will collide perpendicular to the surface. The pressure resistance coefficient is the lowest at the hull of the ship after the bow and will get a little bit higher at the stern of the ship.

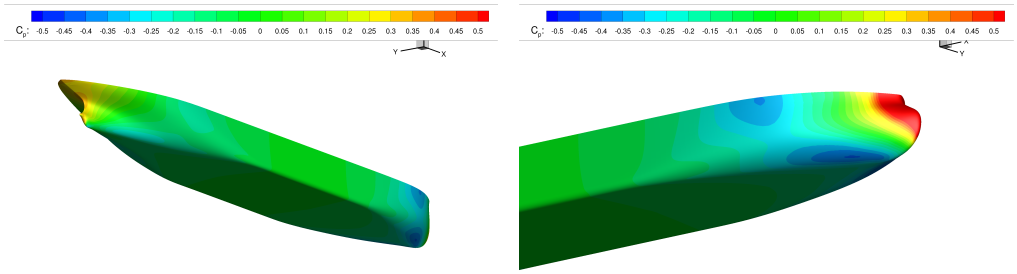

(a) Pressure force at the bow of the ship *(b) Pressure force at the bow of the ship*

Figure 14: Simulation results of the pressure coefficient

4.2.1 Grid study

As the grid is refined (grid cells become smaller and the number of cells in the flow domain increase) the spatial discretization should asymptotically approaches zero, excluding round-off error. A method for examining the convergence of CFD simulations is presented in section 2.5. The uncertainties of the solution for C_F and C_P at the finest grid are examined to determine the quality of the grids and the possibility to get a converged solution for a specific value for y^+.

Figure 15 presents the friction resistance coefficient C_F as a function of the typical cell size ratio $\frac{h_i}{h_1}$. In the bufferlayer, $y_m^+ = 5.4$ is the only value which shows monotonic convergence. For the log-law region ($y_m^+ > 30 - 50$), every value show monotonic convergence, except for $y_m^+ = 1805.8$. The order of convergence p can only be determined for $y_m^+ = 51.9$ and $y_m^+ = 259.6$, which are 0.74 and 1.57, respectively. There is a high uncertainty for the solutions in the viscous sublayer ($y_m^+ < 5$) and the buffer layer ($5 < y_m^+ < 50$). This means that the solution in this region is really dependent on the grid resolution.

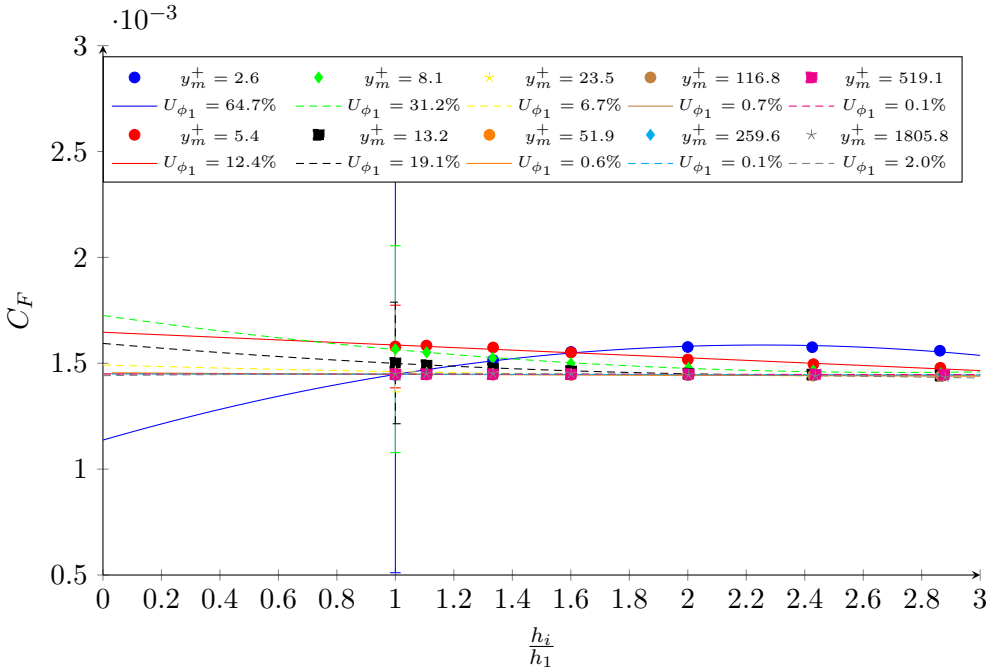

Figure 15: C_F as a function of $\frac{h_i}{h_1}$

Figure 16 shows a closer look on the solution in the log-law region ($y_m^+ > 30 - 50$), where clearly can be seen that the uncertainty is a lot smaller compared to the uncertainty outside the log-law region.

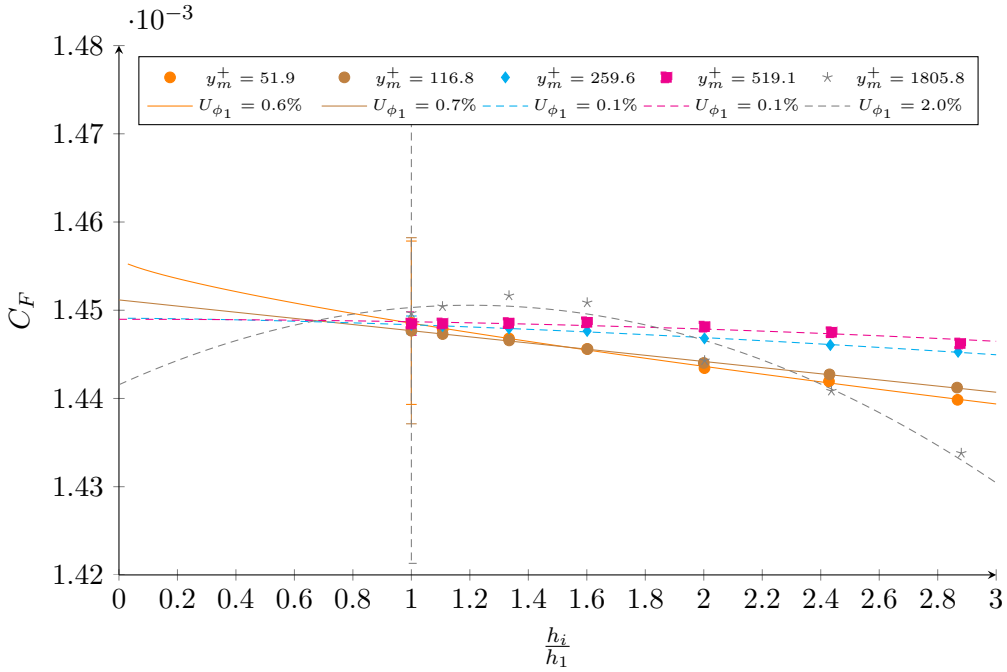

Figure 16: C_F as a function of $\frac{h_i}{h_1}$ for the log-law region only

Figure 17 presents the pressure resistance coefficient C_P as a function of the typical cell size ratio $\frac{h_i}{h_1}$. All solutions show monotonic convergence, except for $y_m^+ = 2.6$. The order of convergence p can only be determined for $y_m^+ = 519.1$, which is $p = 2.0$. The uncertainties are ranging from 4.6% to 13.7% in the bufferlayer ($5 < y_m^+ < 30 - 50$) and the log-law region ($y_m^+ > 30 - 50$), where the uncertainty is a lot higher in the viscous sublayer ($y_m^+ < 5$), i.e.

81.4%. The solution for C_P is very grid dependent for every value of y_m^+.

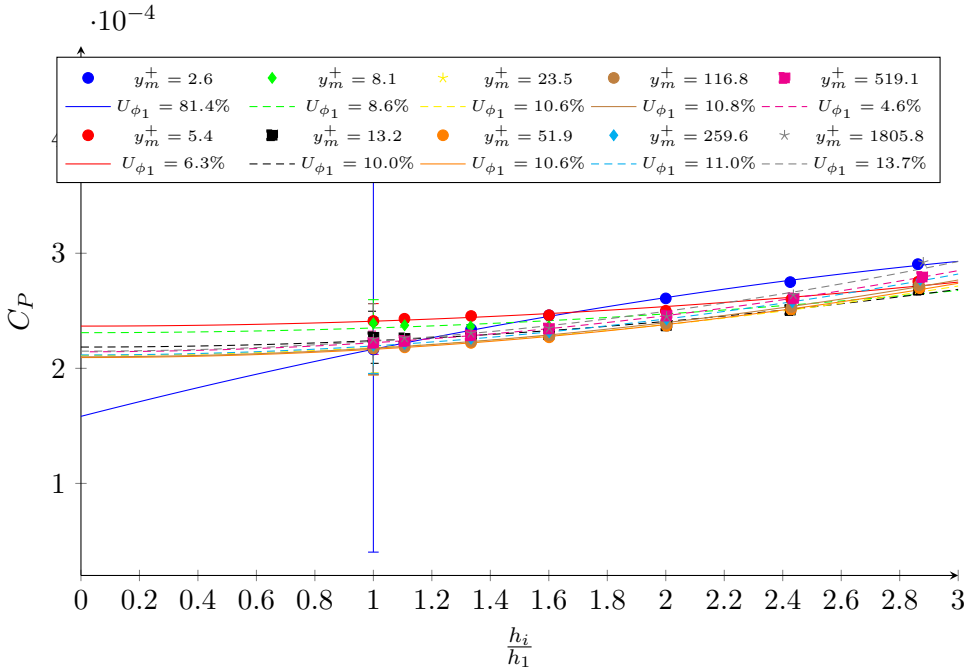

Figure 17: C_P as a function of $\frac{h_i}{h_1}$

4.2.2 Friction resistance coefficient

Figure 18 presents the friction resistance coefficient C_F as a function of y_m^+ for different grid resolutions. As in figure 15 it can easily be seen that there is a region $y_m^+ > 100$ where the uncertainty is relatively lower in comparison with the region $y_m^+ < 100$ and therefore the solution is not particular dependent of the grid resolution.

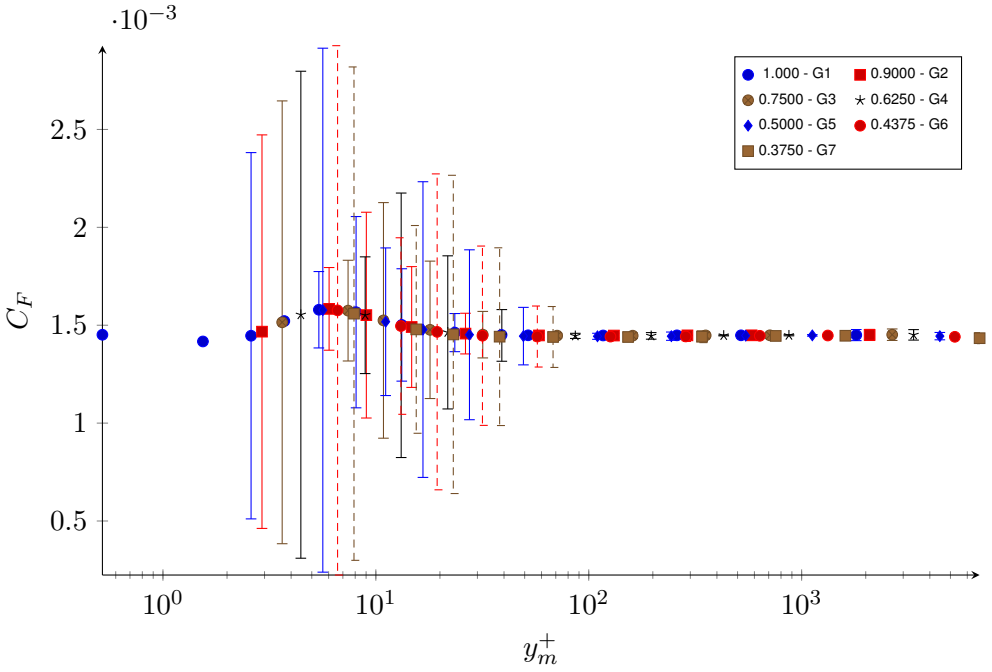

Figure 18: C_F as a function of y_m^+ for different grid resolutions

Figure 19 presents the friction resistance coefficient C_F as a function of y_m^+ for the finest grid

G1. The result obtained with the direct application of the no slip condition (NS) is used as a reference for ΔC_F. It can be seen that the highest uncertainties are seen in the bufferlayer ($5 < y^+ < 30 - 50$) and that the uncertainties in the log-law region are neglectable compared to these in the bufferlayer.

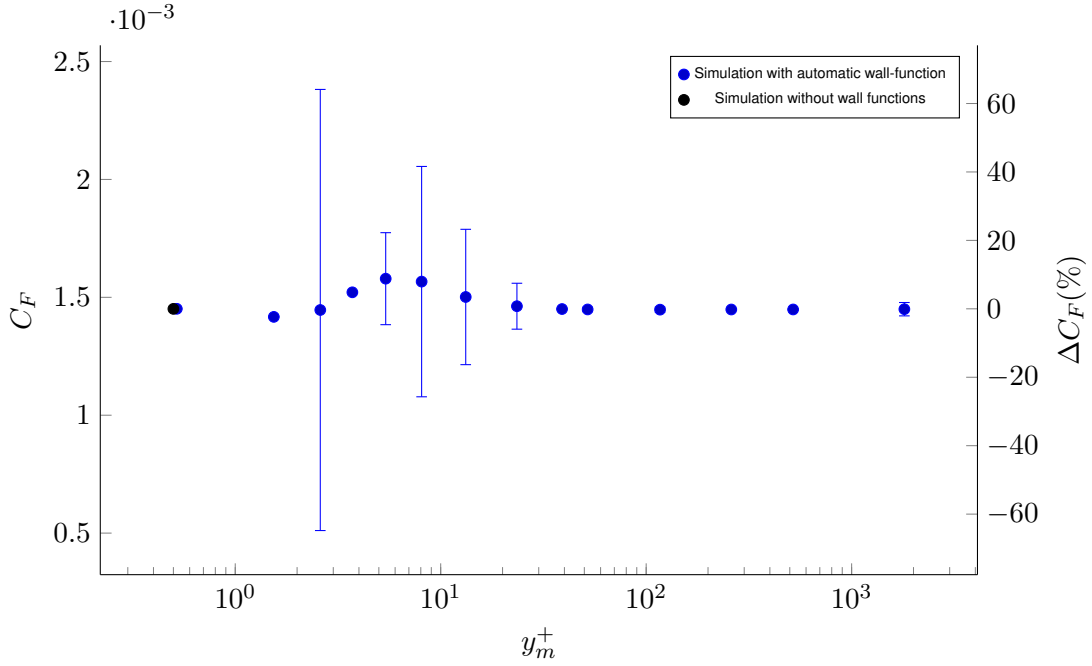

Figure 19: C_F as a function of y_m^+ for the finest grid G1

Figure 20 presents the friction resistance coefficient C_F as a function of y_m^+ for the finest grid G1, but now without the uncertainty bars. The solutions found in the bufferlayer ($5 < y^+ < 30 - 50$) show a high deviation with the no slip condition (up to about 9%), where for the solutions in the viscous sublayer ($y^+ < 5$) and the log law region ($y+ > 30 - 50$) the maximum difference is about 0.3%.

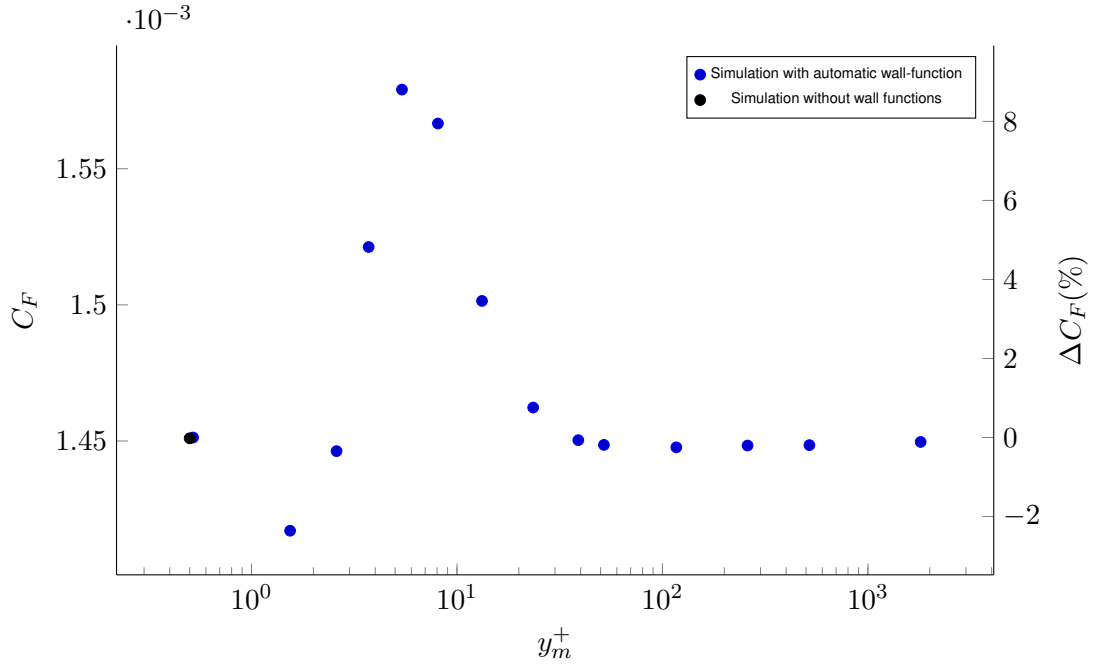

Figure 20: C_F as a function of y_m^+ for the finest grid G1 without uncertainty bars

4.2.3 Pressure resistance coefficient

Figure 21 presents the pressure resistance coefficient C_P as a function of y_m^+ for different grid resolutions. As in figure 17 it can be seen that the solution is really grid dependent for every value of y_m^+.

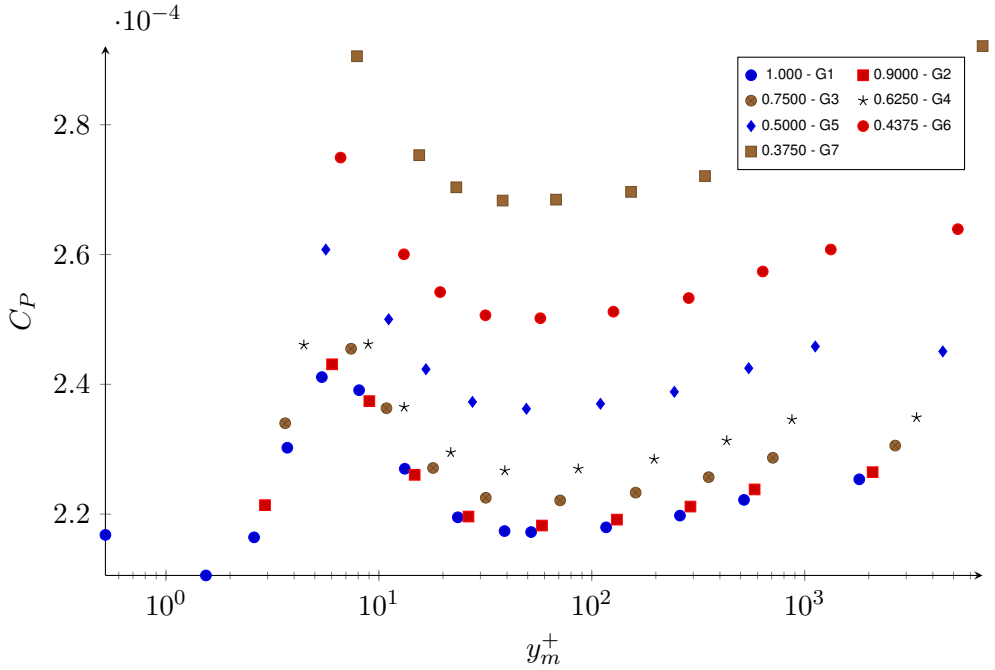

Figure 21: C_P as a function of y_m^+ for different grid resolutions

Figure 22 presents the pressure resistance coefficient C_P as a function of y_m^+ for the finest grid G1. The result obtained with the direct application of the no slip condition (NS) is used as a reference for ΔC_P. As seen before, the numerical uncertainty is high for every value of y_m^+. Almost all changes in C_P are smaller than the estimated numerical uncertainties.

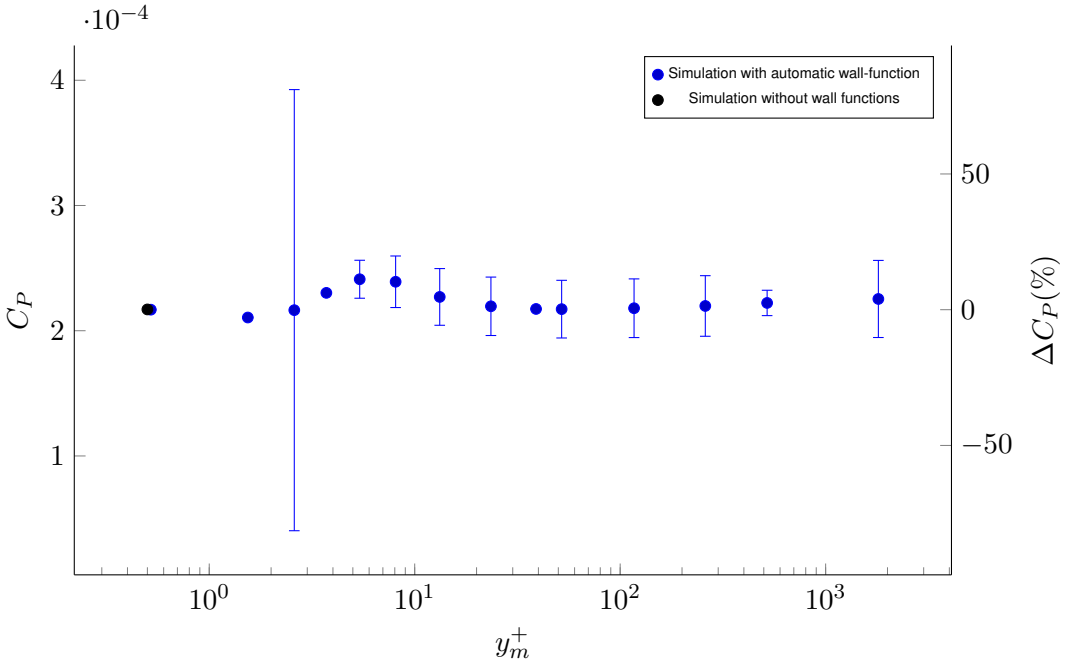

Figure 22: C_P as a function of y_m^+ for the finest grid G1

Figure 22 presents the pressure resistance coefficient C_P as a function of y_m^+ for the finest grid G1, but now without the uncertainty bars. It can be seen that the solution of C_P also is dependent of the value of y_m^+. Especially in the bufferlayer ($5 < y^+ < 30 - 50$), where a difference with the no slip condition of 11% occurs. The viscous sublayer ($y_m^+ < 5$) and the log-law region ($y_m^+ > 30 - 50$) shows a maximum deviation of 4%. Where for C_F the values in the log-law region are roughly constant, it can be seen that for C_P the values increase with growing y_m^+. It could be possible that at certain regions on the hull, the local y^+ is too high to give good results of the local pressure at that region, influencing the overall pressure resistance coefficient. Further research has to be done to determine why this values are increasing with growing y_m^+.

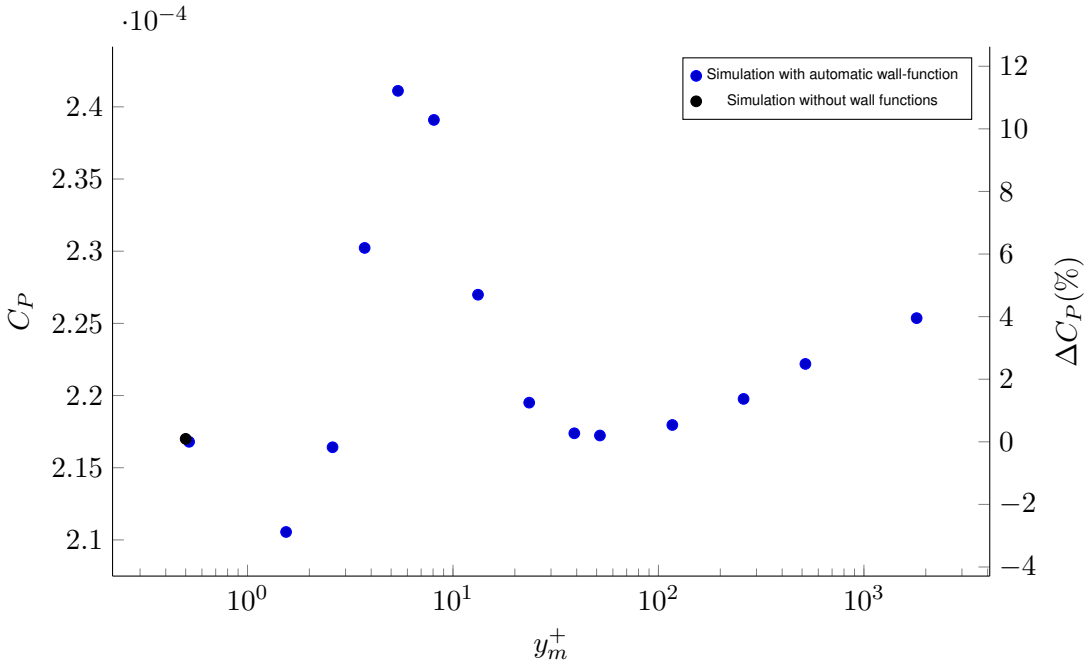

Figure 23: C_P as a function of y_m^+ for the finest grid G1 without uncertainty bars

4.3 Hexpress results

Simulations are also done with grids made with Hexpress to compare the results with those of the simulations done with grids made with Gridpro. Due to the lack of time, no grid study is done to determine the quality of the grids. Besides that, only two kind of grids examined, where for the coarse grid only simulations are done for y^+ values in the log-law region. First, a comparison between the fine and coarse grid is made. After that, the results of the fine Hexpress grid is compared to the results of the finest Gridpro grid.

4.3.1 Resistance coefficients

Figure 24 presents the friction resistance coefficient C_F as a function of y_m^+ for different grid resolutions. It can be seen that the solutions with Hexpress grids in the log-law region ($y_m^+ > 30 - 50$) are more grid dependent as for solutions with Gridpro grids. It can also be seen that the solution in the log-law region is decreasing with growing y_m^+ for the 3511k grid and increasing for the 944k grid. It also had to be noted that with increasing y_m^+, the amount of grid cells are decreasing more than with the Gridpro grids, which possibly can explain the increase in deviation between the values at high y_m^+.

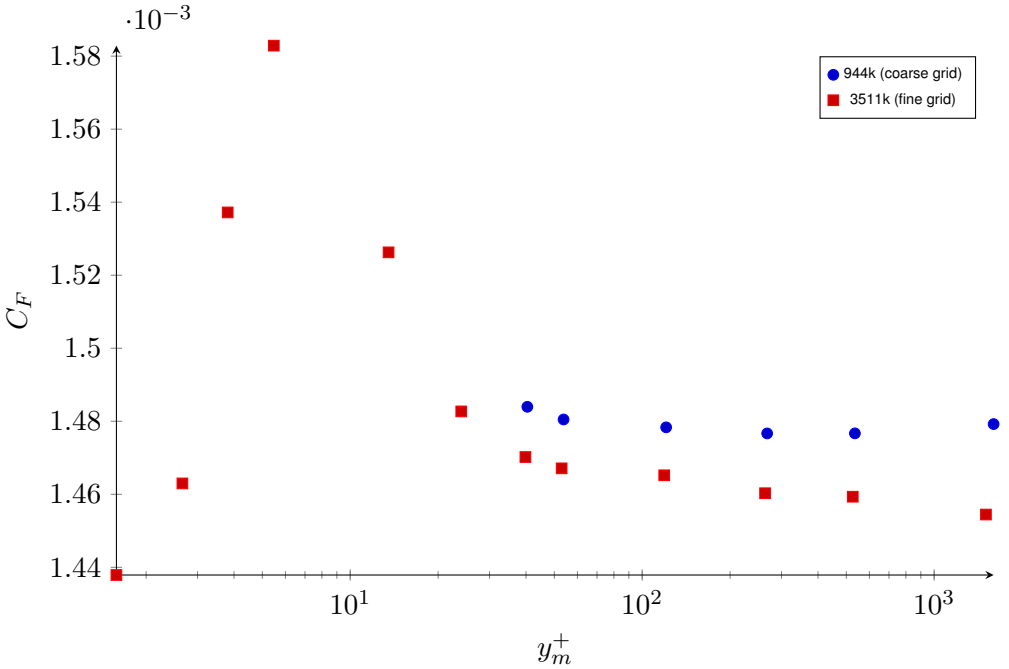

Figure 24: C_F as a function of y_m^+ for different grid resolutions

Figure 25 presents the friction resistance coefficient C_F as a function of y_m^+ for the finest Hexpress grid and the finest Gridpro grid. The solution with the Hexpress grids show the same behaviour as for the solution with the Gridpro grid: it will increase substantially in the bufferlayer ($5 < y_m^+ < 30 - 50$) in comparison with the viscous sublayer ($y_m^+ < 5$) and the log-law region ($y_m^+ > 30 - 50$). From the behaviour of figure 24, it is expected that a finer Hexpress grid will result in a solution for C_F closer to that of grids made with Gridpro.

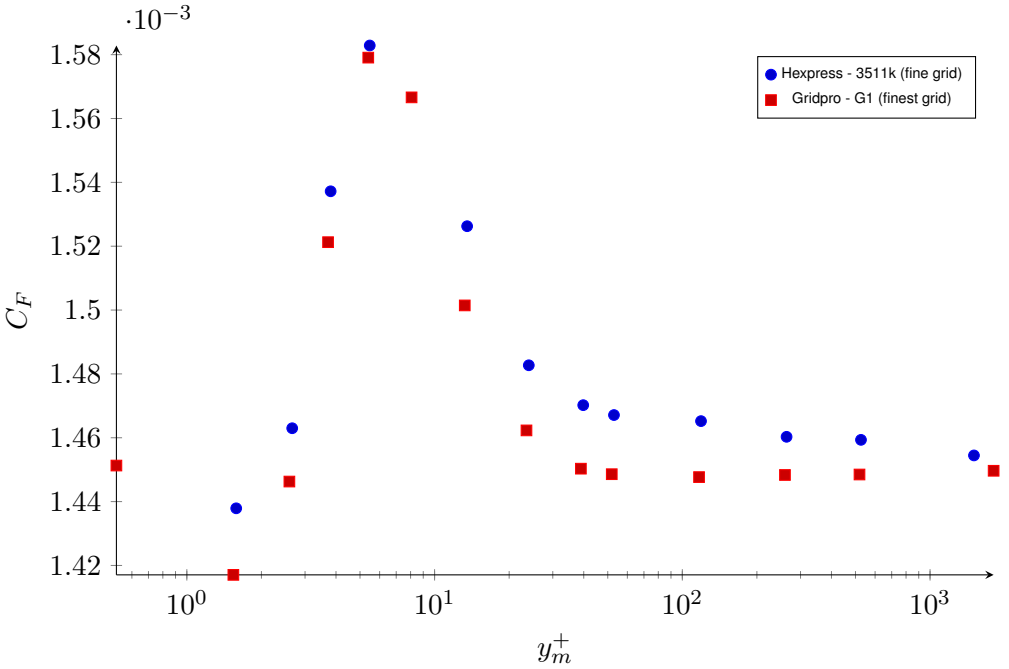

Figure 25: C_F as a function of y_m^+ for the finest Hexpress grid and the finest Gridpro grid

Figure 26 presents the pressure resistance coefficient C_P as a function of y_m^+ for different grid resolutions. The solution for $y_m^+ = 52.98$ shows a small unexpected increase. It is unknown yet why this sudden increase occurs at this value. Also a substantial deviation between both

grids is observed. From the results of the simulations with the Gridpro grids, it is known that the solution for C_P is highly grid dependent. It is therefore assumed that this is also the case for the Hexpress grids. Further research by using more grids is essential to confirm this assumption.

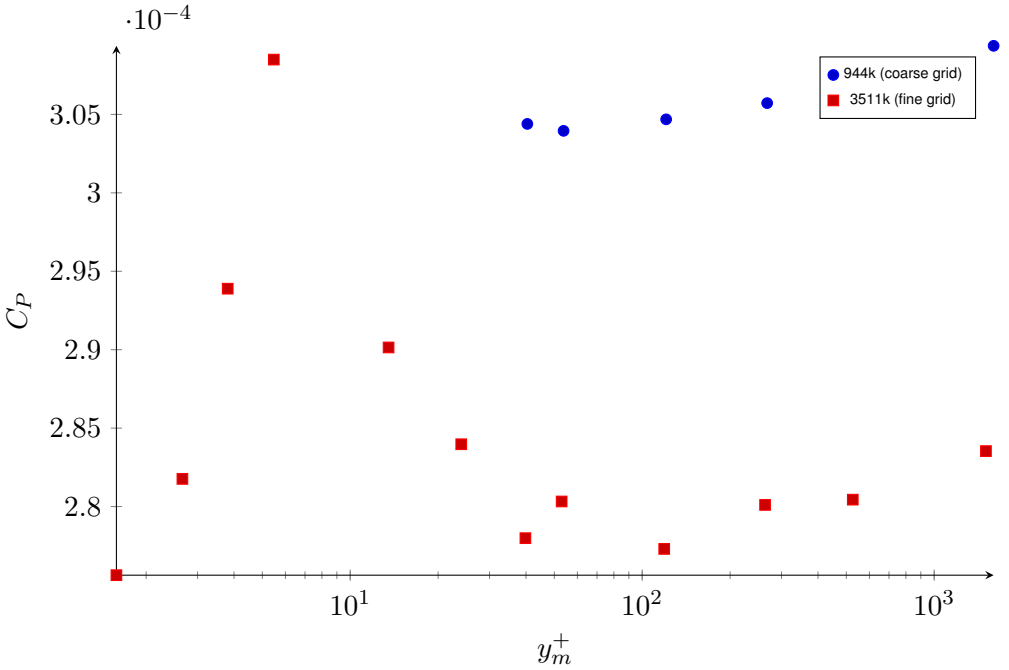

Figure 26: C_P as a function of y_m^+ for different grid resolutions

Figure 27 presents the pressure resistance coefficient C_P as a function of y_m^+ for the finest Hexpress grid and the finest Gridpro grid. The same behaviour for the solution is observed for both the Hexpress grid and the Gridpro grid: it will increase substantially in the bufferlayer ($5 < y_m^+ < 30 - 50$) in comparison with the viscous sublayer ($y_m^+ < 5$) and the log-law region ($y_m^+ > 30 - 50$) and in the solution increases with growing y_m^+ in the log-law region.

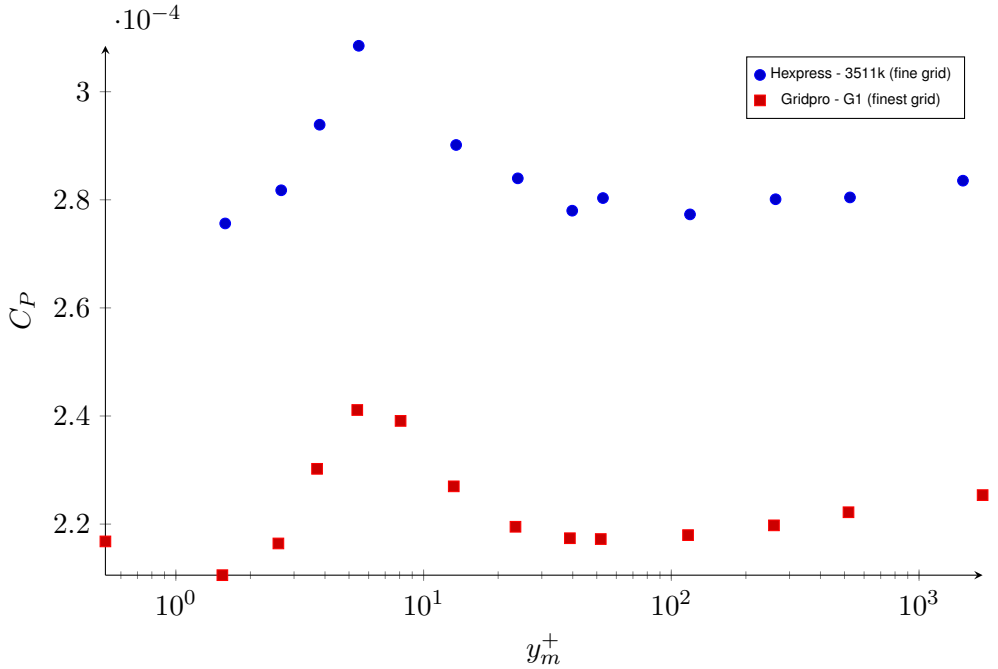

Figure 27: C_P as a function of y_m^+ for the finest Hexpress grid and the finest Gridpro grid

5 CONCLUSIONS

One approach to describe the solution of the shear-stress at a wall is the application of wall functions which determine the shear-stress at the wall from semi-empirical equations. The y^+ is the dimensionless quantity for the distance from the wall up to the centre of the first grid cell. In simulations without wall functions, this quantity is typically around 1, while wall functions allow us to take a y^+ higher than 1. The boundary layer can be divide in two region: the inner layer and the outer layer. The former also consist of three regions, which are from the wall up to the outer layer: the viscous sublayer ($y^+ < 5$), the buffer layer ($5 < y^+ < 30 - 50$) and the log-law region ($y^+ > 30 - 50$).

From the CFD simulations done with the Gridpro grids it follows that the solutions for the pressure resistance coefficient C_P and the friction resistance coefficient C_F with an y^+ in the log-law region give the best results. These solution are the closest to the solutions without applying wall functions. Simulations with an y^+ in the viscous sublayer also give satisfactory results based on the deviation with the solution without applying wall functions, but only on the finest grid, which can be seen by the high uncertainty value for this specific y^+. The best results are gained with an y^+ between 50 and 100, based on the pressure resistance coefficient C_P. This is because the deviation to the solution without applying wall functions is increasing after $y^+ = 100$.

5.1 Recommendations

It has to be noted that this conclusion is based on simulations done for only one geometry and a particular configuration of the flow. It is recommended to repeat this study for other geometries and configurations as well, to see if this conclusion still applies.

Due to the lack of time, only a limited amount of simulations with Hexpress grids are done. It is therefore unknown how well the solutions on those grids are converged. The recommendation is to generate at least two more grids with several values for y^+ in every region of the inner layer, e.g. viscous sublayer, buffer layer and log-law region.

It is also not yet known why the values of C_P increase with growing y^+ for simulation with both Gridpro grids and Hexpress grids. It could be due to some regions with a higher local y^+, causing some higher pressures, influencing the integrated pressure. This can easily be seen by plotting the pressure distribution over the hull. Due to lack of time, this was not possible to include in this study.

REFERENCES

[1] BL Jensen, BM Sumer, HR Jensen, and J Fredsoe. Flow around and forces on a pipeline near a scoured bed in steady current. *Journal of Offshore Mechanics and Arctic Engineering*, 112(3):206–213, 1990.

[2] John Kim, Parviz Moin, and Robert Moser. Turbulence statistics in fully developed channel flow at low reynolds number. *Journal of fluid mechanics*, 177:133–166, 1987.

[3] L. Larsson, F. Stern, and Bertram V. Eds. In *Proceedings Gothenburg 2000 A Workshop on Numerical Ship Hydrodynamics*, September 2010.

[4] L. Larsson, F. Stern, and M. Visonneau. Eds. In *Proceedings Gothenburg 2000 A Workshop on Numerical Ship Hydrodynamics*, December 2010.

[5] Joel H Ferziger and Milovan Perić. *Computational methods for fluid dynamics*, volume 3. Springer Berlin, 2002.

[6] Stephen B Pope. *Turbulent flows*. Cambridge university press, 2000.

[7] O. Reynolds. On the dynamical theory of incompressible viscous fluids and the determination of the criterion. *Philosophical Transactions of the Royal Society of London*, 186:123–164, 1895.

[8] David C Wilcox et al. *Turbulence modeling for CFD*, volume 2. DCW industries La Canada, CA, 1998.

[9] Joseph Boussinesq. *Essai sur la théorie des eaux courantes*, volume 2. Imprimerie nationale, 1877.

[10] N.C. Markatos. The mathematical modelling of turbulent flows. *Applied Mathematical Modelling*, 10(3):190 – 220, 1986.

[11] B.E. Launder and B.I. Sharma. Application of the energy-dissipation model of turbulence to the calculation of flow near a spinning disc. *Letters in Heat and Mass Transfer*, 1(2):131 – 137, 1974.

[12] David C Wilcox. Reassessment of the scale-determining equation for advanced turbulence models. *AIAA journal*, 26(11):1299–1310, 1988.

[13] W Rodi and G Scheuerer. Scrutinizing the k-ε turbulence model under adverse pressure gradient conditions. *Journal of fluids engineering*, 108(2):174–179, 1986.

[14] FR Menter. Influence of freestream values on k-omega turbulence model predictions. *AIAA journal*, 30(6):1657–1659, 1992.

[15] Florian R Menter. Two-equation eddy-viscosity turbulence models for engineering applications. *AIAA journal*, 32(8):1598–1605, 1994.

[16] FR Menter, M Kuntz, and R Langtry. Ten years of industrial experience with the sst turbulence model. *Turbulence, heat and mass transfer*, 4(1), 2003.

[17] B. E. Launder and D. B. Spalding. *Lectures in Mathematical Models of Turbulence*. Academic Press, London, England, 1972.

[18] L. Prandtl. Bericht über die entstehung der turbulenz. *Z. Angew. Math. Mech. 5*, pages 136 – 139, 1925.

[19] Th. von Kármán. Mechanische Ähnlichkeit und Turbulenz. *Nachrichten von der Gesellschaft der Wissenschaften zu Göttingen*, pages 58–76, 1930.

[20] F. Menter and T. Esch. Elements of industrial heat transfer predictions. *16th Brasilian Congress of Mechanical Engineering*, 2001.

[21] L. Eca and M. Hoekstra. Verification and validation for marine applications of cfd. In *Proceedings of 29th Symposium on Naval Hydrodynamics (ONR)*, Gothenburg, Sweden, August 2012.

[22] SL Toxopeus, CD Simonsen, E Guilmineau, M Visonneau, T Xing, and F Stern. Investigation of water depth and basin wall effects on kvlcc2 in manoeuvring motion using viscous-flow calculations. *Journal of Marine Science and Technology*, 18(4):471–496, 2013.

[23] AH Koop, CM Klaij, and G Vaz. Viscous-flow calculations for model and full-scale current loads on typical offshore structures. In *MARINE 2011, IV International Conference on Computational Methods in Marine Engineering*, pages 3–29. Springer, 2013.

[24] D Rijpkema and G Vaz. Viscous flow computations on propulsors: verification, validation and scale effects. *Proceedings of the Developments in Marine CFD*, 2011.

[25] Windt J. Adaptive mesh refinement in viscous flow solvers: Refinement in the near-wall region, implementation and verification. In *Proceedings of NUTTS2013*, Mulheim, Germany, 2013.

[26] Maarten Kerkvliet, Guilherme Vaz, Nicolas Carette, and Michiel Gunsing. Analysis of u-type anti-roll tank using urans: Sensitivity and validation. In *ASME 2014 33rd International Conference on Ocean, Offshore and Arctic Engineering*, pages V002T08A031–V002T08A031. American Society of Mechanical Engineers, 2014.

[27] B. Schuiling. The design and numerical demonstration of a new energy saving device. In *Proceedings of NUTTS2013*, Mulheim, Germany, 2013.

[28] Guilherme Vaz, Frederick Jaouen, and Martin Hoekstra. Free-surface viscous flow computations: Validation of urans code fresco. In *ASME 2009 28th International Conference on Ocean, Offshore and Arctic Engineering*, pages 425–437. American Society of Mechanical Engineers, 2009.

[29] CM Klaij and C Vuik. Simple-type preconditioners for cell-centered, colocated finite volume discretization of incompressible reynolds-averaged navier–stokes equations. *International Journal for Numerical methods in fluids*, 71(7):830–849, 2013.

[30] F Menter and T Esch. Elements of industrial heat transfer predictions. In *16th Brazilian Congress of Mechanical Engineering (COBEM)*, pages 26–30, 2001.

[31] Patrick J Roache. *Verification and validation in computational science and engineering*. Hermosa, 1998.

[32] Luis Eça and Martin Hoekstra. A procedure for the estimation of the numerical uncertainty of cfd calculations based on grid refinement studies. *Journal of Computational Physics*, 262:104–130, 2014.

[33] L. Eça, G. Vaz, and M. Hoekstra. Code verification, solution verification and validation in rans solvers. In *Proceedings of the International Conference on Offshore Mechanics and Arctic Engineering - OMAE*, volume 6, pages 597–605, 2010.

[34] Patrick J Roache. *Fundamentals of verification and validation*. hermosa publ., 2009.

[35] Eća L. and Hoekstra M. On the application of wall functions in ship viscous flows. *International Conference on Computational Methods in Marine Engineering*, 2011.

[36] Herrmann Schlichting, Klaus Gersten, and Klaus Gersten. *Boundary-layer theory*. Springer Science & Business Media, 2000.

APPENDIX I

Turbulence models

$k-\varepsilon$ Model

For this model the turbulent viscosity (or eddy viscosity) is defined as:

$$\nu_t = \frac{C_\mu k^2}{\varepsilon} \tag{36}$$

Where k^2 represents the turbulence velocity scale and ε is the turbulent dissipation rate and is associated with the turbulent length scale l by means of:

$$\varepsilon = \frac{C_\mu k^{\frac{3}{2}}}{l} \tag{37}$$

The equations and coefficients that define this model are:

- Turbulent kinetic energy k equation:

$$\frac{\partial k}{\partial t} + u_j \frac{\partial k}{\partial x_j} = \tau_{ij} \frac{\partial u_i}{\partial x_j} - \varepsilon + \frac{\partial}{\partial x_j}\left[\left(\nu + \frac{\nu_t}{\sigma_k}\right)\frac{\partial k}{\partial x_j}\right] \tag{38}$$

- Dissipation rate ε equation:

$$\frac{\partial \varepsilon}{\partial t} + u_j \frac{\partial \varepsilon}{\partial x_j} = C_{\varepsilon 1}\frac{\varepsilon}{k}\tau_{ij}\frac{\partial u_i}{\partial x_j} - C_{\varepsilon 2}\frac{\varepsilon^2}{k} + \frac{\partial}{\partial x_j}\left[\left(\nu + \frac{\nu_t}{\sigma_\varepsilon}\right)\frac{\partial \varepsilon}{\partial x_j}\right] \tag{39}$$

- Closure coefficients and auxiliary relations:

$$C_{\varepsilon 1} = 1.44, \quad C_{\varepsilon 2} = 1.92, \quad C_\mu = 0.09, \quad \sigma_k = 1.0, \quad \sigma_\varepsilon = 1.3 \tag{40}$$

The term $\tau_{ij}\frac{\partial u_i}{\partial x_j}$ is also called rate of production of turbulent kinetic energy, usually denoted by P_k, which according the assumption of the eddy-viscosity model (equation (13)), is calculated using:

$$P_k = \tau_{ij}\frac{\partial u_i}{\partial x_j} = 2\nu_t S_{ij}\frac{\partial u_i}{\partial x_j} = \nu_t\left(\frac{\partial u_i}{\partial x_j} + \frac{\partial u_j}{\partial x_i}\right)\frac{\partial u_i}{\partial x_j} \tag{41}$$

For this model, at a wall $k = 0$ and $\varepsilon = 0$.

$k-\omega$ Model

For this model the turbulent viscosity (or eddy viscosity) is defined as:

$$\nu_t = \frac{k}{\omega} \tag{42}$$

The equations and coefficients that define this model are:

- Turbulent kinetic energy k equation:

$$\frac{\partial k}{\partial t} + u_j \frac{\partial k}{\partial x_j} = \tau_{ij} \frac{\partial u_i}{\partial x_j} - \beta^* k\omega + \frac{\partial}{\partial x_j}\left[\left(\nu + \frac{\nu_t}{\sigma^*}\right)\frac{\partial k}{\partial x_j}\right] \tag{43}$$

- Specific dissipation rate ω equation:

$$\frac{\partial \omega}{\partial t} + u_j \frac{\partial \omega}{\partial x_j} = \alpha \frac{\omega}{k} \tau_{ij} \frac{\partial u_i}{\partial x_j} - \beta\omega^2 + \frac{\partial}{\partial x_j}\left[\left(\nu + \frac{\nu_t}{\sigma^*}\right)\frac{\partial \omega}{\partial x_j}\right] \tag{44}$$

- Closure coefficients and auxiliary relations:

$$\alpha = \frac{5}{9}, \quad \beta = \frac{3}{40}, \quad \beta^* = \frac{9}{100}, \quad \sigma = \frac{1}{2}, \quad \sigma^* = \frac{1}{2} \tag{45}$$

By means of an asymptotic analysis close to the wall, there can be a limit and boundary condition for ω determined. Considering Δ_y to be the distance between the first point and the wall, the boundary conditions for the model at the wall are:

$$k = 0, \quad \omega = 10\frac{6\nu}{\beta(\Delta_y)^2} \tag{46}$$

For external conditions, i.e. outside the boundary layer, the following relations are given:

$$\omega_\infty = \lambda \frac{U_{ref}}{L_{ref}}, \quad \nu_\infty = 10^{-3}\nu, \quad k_\infty = \nu_{t\infty}\omega_\infty \tag{47}$$

Where U_{ref} and L_{ref} are reference quantities and λ is a parameter that can vary from 1 to 10. This model is said to present advantages when compared with the most used $k-\varepsilon$ models. Its simple formulation for the sub-viscous layer and the decoupling between the k and ω render numerically robust model.

$k-\omega$ SST Menter Model (1994)

The turbulent viscosity is here considered to be:

$$\mu_t = \frac{\frac{\rho k}{\omega}}{\max\left(1, \frac{\Omega F_2}{a_1 \omega}\right)}, \quad a_1 = 0.31 \tag{48}$$

Where Ω represents the flow vorticity. The auxiliary function F_2 is defined by means of the wall distance d,

$$F_2 = \tanh\left\{\left[\max\left(2\frac{\sqrt{k}}{0.09 d\omega}, \frac{500\mu}{\rho d^2 \omega}\right)\right]^2\right\} \tag{49}$$

The transport equation include also an auxiliary function F_1, which performs a transition between the $k-\omega$ original model and the $k-\varepsilon$ model for the shear zones and the external zones. The equations and coefficients that define the model are then:

- Turbulent kinetic energy k equation:

$$\frac{\partial \rho k}{\partial t} + \frac{\partial}{\partial x_j}\left(\rho u_j k - (\mu + \sigma_k \mu_t)\frac{\partial k}{\partial x_j}\right) = \tau_{ij} S_{ij} - \beta^* \rho \omega k \tag{50}$$

- Specific dissipation rate ω equation:

$$\frac{\partial \rho \omega}{\partial t} + \frac{\partial}{\partial x_j}\left(\rho u_j \omega - (\mu + \sigma_\omega \mu_t)\frac{\partial \omega}{\partial x_j}\right) = \gamma \rho \Omega^2 - \beta \rho \omega^2 + 2(1 - F_1)\frac{\rho \sigma_{w2}}{\omega}\frac{\partial k}{\partial x_j}\frac{\partial \omega}{\partial x_j} \tag{51}$$

- Closure coefficients and auxiliary relations:

$$F_1 = \tanh\left\{\left[\min\left[\max\left(2\frac{\sqrt{k}}{0.09 d\omega}, \frac{500\mu}{\rho d^2 \omega}\right), \frac{4\rho\sigma_{w2}\kappa}{CD_{k\omega} d^2}\right]\right]^4\right\} \tag{52a}$$

$$CD_{k\omega} = \max\left(\frac{2\rho\sigma_{w2}}{\omega}\frac{\partial k}{\partial x_j}\frac{\partial \omega}{\partial x_j}, 1 \times 10^{-20}\right) \tag{52b}$$

$$a_1 = 0.31, \quad \beta^* = 0.09, \quad \kappa = 0.41 \tag{52c}$$

The coefficients β, γ, σ_k and σ_w are defined by a transition between the coefficients of the original model (denoted by 1) and a $k - \varepsilon$ transformed model (denoted by 2).

$$\phi = F_1 \phi_1 + (1 - F_1)\phi_2, \quad \phi = \{\beta, \gamma, \sigma_k, \sigma_w\} \tag{53}$$

With the coefficients given by:

$$\begin{aligned} &\sigma_{k1} = 0.85, \quad \sigma_{\omega 1} = 0.50, \quad \beta_1 = 0.075, \quad \gamma_1 = \frac{\beta_1}{\beta^*} - \frac{\sigma_{\omega 1} K^2}{\sqrt{\beta^*}} = 0.553, \\ &\sigma_{k2} = 1.00, \quad \sigma_{\omega 2} = 0.856, \quad \beta_2 = 0.0828, \quad \gamma_2 = \frac{\beta_2}{\beta^*} - \frac{\sigma_{\omega 2} K^2}{\sqrt{\beta^*}} = 0.440 \end{aligned} \tag{54}$$

The limiting conditions for the $k-\omega$ SST Menter model are the same as the ones for the $k-\omega$ model.

$k - \omega$ SST Menter Model (2003)

The only difference between this model and the model from 1994 is the turbulent eddy viscosity and the use of the factor 10 in the production limiter, instead of 20. The turbulent eddy viscosity is now defined as:

$$\nu_t = \frac{a_1 k}{\max(a_1 \omega, S, F_2)} \tag{55}$$

And the new expression for $CD_{k\omega}$:

$$CD_{k\omega} = \max\left(\frac{2\rho\sigma_{w2}}{\omega}\frac{\partial k}{\partial x_j}\frac{\partial \omega}{\partial x_j}, 1 \times 10^{-10}\right) \tag{56}$$

APPENDIX II

ReFRESCO

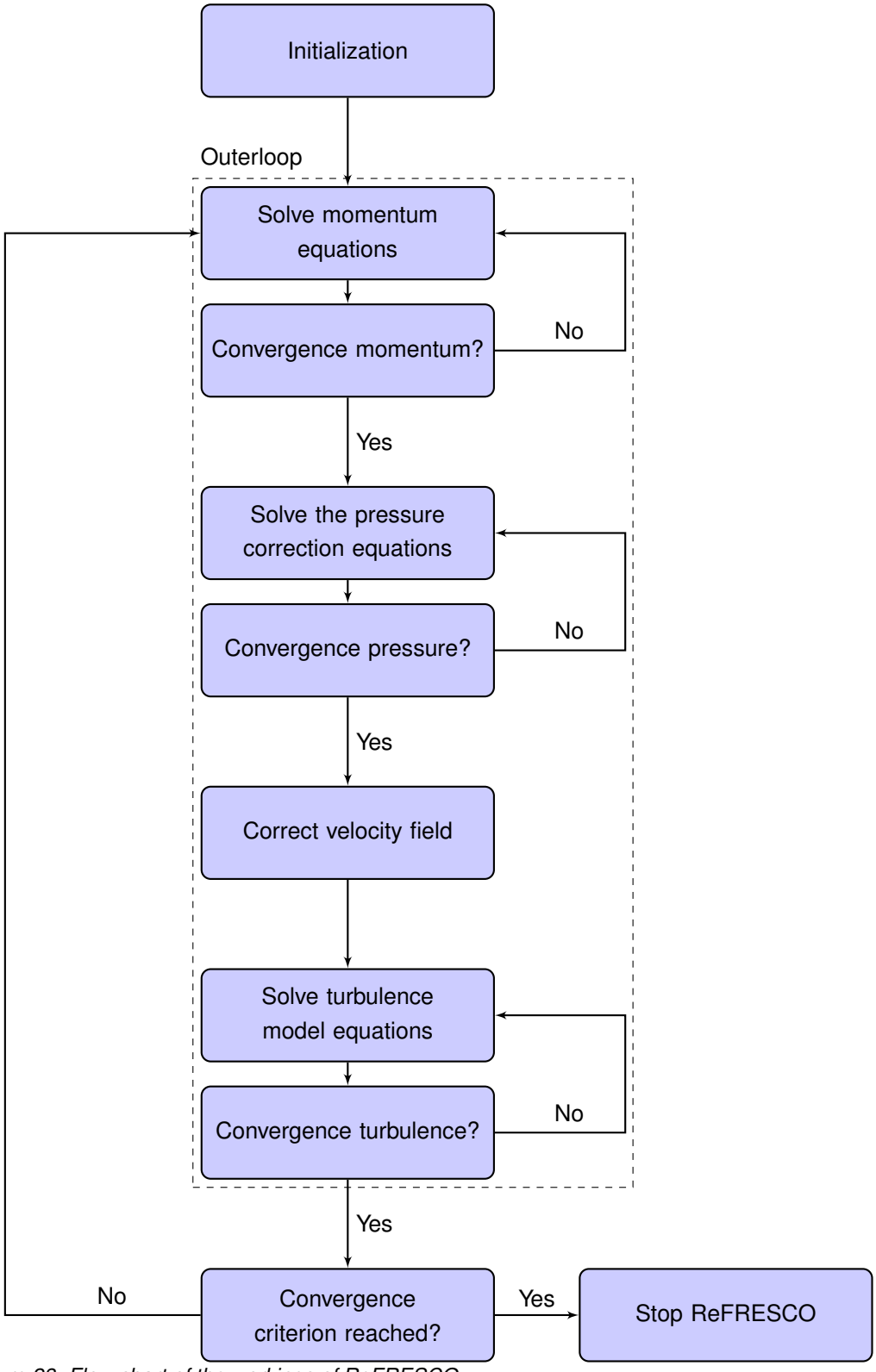

Figure 28: Flow chart of the workings of ReFRESCO

APPENDIX III

Numerical uncertainty

The equation presented below are valid for least-squares solution with and without weights.

- Non-weighted approach

$$w_i = 1 \qquad \text{and} \qquad nw_i = 1 \tag{57}$$

- Weighted approach

$$w_i = \frac{\frac{1}{h_i}}{\sum_{i=1}^{n_g} \frac{1}{h_i}} \qquad \text{and} \qquad nw_i = n_g w_i \tag{58}$$

Single term expansion with unknown order of grid convergence

ϕ_0, α and p are determined from the minimum of the function:

$$S_{RE}(\phi_0, \alpha, p) = \sqrt{\sum_{i=1}^{n_g} w_i \left(\phi_i - (\phi_0 + \alpha h_i^p)\right)^2} \tag{59}$$

With standard deviation:

$$\sigma_{RE} = \sqrt{\frac{\sum_{i=1}^{n_g} \left(\phi_i - (\phi_0 + \alpha h_i^p)\right)^2}{n_g - 3}} \tag{60}$$

Single term expansion with first-order term

ϕ_0 and α are determined from the minimum of the function:

$$S_1^w(\phi_0, \alpha) = \sqrt{\sum_{i=1}^{n_g} w_i \left(\phi_i - (\phi_0 + \alpha h_i)\right)^2} \tag{61}$$

With standard deviation:

$$\sigma_1 = \sqrt{\frac{\sum_{i=1}^{n_g} \left(\phi_i - (\phi_0 + \alpha h_i)\right)^2}{n_g - 2}} \tag{62}$$

Single term expansion with second-order term

ϕ_0 and α are determined from the minimum of the function:

$$S_2^w(\phi_0, \alpha) = \sqrt{\sum_{i=1}^{n_g} w_i \left(\phi_i - (\phi_0 + \alpha h_i^2)\right)^2} \tag{63}$$

With standard deviation:

$$\sigma_2 = \sqrt{\frac{\sum_{i=1}^{n_g} \left(\phi_i - (\phi_0 + \alpha h_i^2)\right)^2}{n_g - 2}} \tag{64}$$

Two-term expansion with first and second-order terms

ϕ_0, α_1 and α_2 are determined from the minimum of the function:

$$S_{12}^w(\phi_0, \alpha_1, \alpha_2) = \sqrt{\sum_{i=1}^{n_g} w_i \left(\phi_i - (\phi_0 + \alpha_1 h_i + \alpha_2 h_i^2)\right)^2} \tag{65}$$

With standard deviation:

$$\sigma_{12} = \sqrt{\frac{\sum_{i=1}^{n_g} \left(\phi_i - (\phi_0 + \alpha_1 h_i + \alpha_2 h_i^2)\right)^2}{n_g - 3}} \tag{66}$$

APPENDIX IV

GRIDSIZE

GridPro grids

Table 4: The grid sets and their corresponding number of cells

y^+	0.5	1.5	2.5	3.5	5
y^+_m	0.52	1.54	2.59 - 7.90	3.72	5.40 - 15.48
G1	23482368	22577152	22159360	21880832	21602304
G2	-	-	16350635	-	15953161
G3	-	-	9328896	-	9093888
G4	-	-	5403200	-	5267200
G5	-	-	2769920	-	2700288
G6	-	-	1552785	-	1506089
G7	-	-	945043	-	919897

Table 5: The grid sets and their corresponding number of cells

y^+	7.5	12.5	22.5	37.5	50
y^+_m	8.08 - 23.11	13.24 - 38.15	23.49 - 67.99	38.96	51.90 - 153.01
G1	21254144	20836352	20418560	20000768	19722240
G2	15669251	15385341	15044649	-	14533611
G3	8976384	8780544	8623872	-	8310528
G4	5185600	5076800	4968000	-	4804800
G5	2648064	2595840	2543616	-	2456576
G6	1482741	1459393	1424371	-	1377675
G7	903133	886369	869605	-	836077

Table 6: The grid sets and their corresponding number of cells

y^+	112.5	250	500	1500
y^+_m	116.84 - 340.52	259.61 - 755.79	519.07 - 1604.69	1805.84 - 6855.05
G1	19095552	19165184	17911808	16379904
G2	14079355	14136137	13227625	12091985
G3	8036352	8075520	7566336	6900480
G4	4641600	4668800	4369600	3988800
G5	2386944	2386944	2230272	2038784
G6	1330979	1330979	1237587	1132521
G7	810931	810931	752257	685201

Hexpress grids

Table 7: The grid sets and their corresponding number of cells

y^+	y_m^+	944k	3511k
1.5	1.58	-	28593385
2.5	2.66	-	26802085
3.5	3.81	-	26204985
5	5.47	-	16044825
12.5	13.53	-	22011525
22.5	24.01	-	19624845
37.5	39.82 - 40.43	5216580	18431505
50	52.98 - 53.79	5064059	17238165
112.5	118.98 - 120.80	4301454	14842925
250	263.55 - 267.90	3687247	11861715
500	526.25 - 535.17	3078031	10067613
1500	1504.10 - 1598.02	2314291	7085640

APPENDIX V

PROCEDURE

This appendix contains information about the procedure used to assess this study. It provides information about how to redo this study with the same test case or with some adjustments for other test cases.

In the root folder there will be several different folders which can be divided in preprocessing (0), Gridpro and Hexpress files (1), grids (2), calculations (3), postprocessing (4), results (5) and report (6).

Preprocessing

The first folder, 0_Preprocessing, contains several bash scripts for preprocessing. The main script to use is create_calc.sh, which creates folders and files for a specific y^+ and grid-size. It can be called from the commandline:

```
sh create_calc.sh <yplus> <grid> <cores> <max-iteration> <Gridpro|Hexpress>
```

This script creates the following folders:

- 2_Grids_<Gridpro|Hexpress>/<yplus>/<grid>
- 2_Grids_<Gridpro|Hexpress>/<yplus>/<grid>/refresco
- 3_Calculations_<Gridpro|Hexpress>/<yplus>/<grid>
- 5_Results_<Gridpro|Hexpress>/<yplus>/<grid>

It also creates the following files:

- 3_Calculations_<Gridpro|Hexpress>/<yplus>/<grid>/controls.xml
- 3_Calculations_<Gridpro|Hexpress>/<yplus>/<grid>/job_refresco.job

The control-file which will be copied is controls_batch_<Gridpro|Hexpress>.xml, which is in the preprocessing folder. This control-file already contains all the correct parameters for the KVLCC2 test case and the scripts adjusts the maximum iterations and the path to the grid. The job-file which will be copied is job_batch.job, which is also in the preprocessing folder. The amount of cores will be adapted with the script.

The following command can be used to call create_calc.sh for every y^+ and grid-size used in this study:

```
sh create_calc_all.sh <max-iteration> <Gridpro|Hexpress>
```

Gridpro and Hexpress files

Gridpro files

The folder 1_Gridpro contains several bash scripts to generate the grids with Gridpro. The folder cleanGrid contains files with a grid from the KVLCC2 topology. The script yplus_grid.sh calls a function of Gridpro to cluster the grid cells at the KVLCC2 hull surface (wall). It can be called from the commandline:

```
sh yplus_grid.sh <walldst> <growth>
```

Where <walldst> is equal to 2 times the y^+ and <growth> is the stretching factor, which has been taken 1.10 in this study. Gridpro also has a function to coarsen the grid. All of this can be done with yplus.sh, which can be called from the commandline:

```
sh yplus.sh <walldst> <growth>
```

This script creates the initial grid (1.000 - G1) and grid which are coarser with coarsening ratio 0.9000 (G2), 0.7500 (G3), 0.6250 (G4), 0.5000 (G5), 0.4375 (G6), 0.3750 (G7), 0.3125 (G8) and 0.2500 (G9).

Hexpress files

The folder 1_Hexpress contains some files to recreate the finest grids made with Hexpress. In the folder 112.5/3511k the .igg-file can be opened and edited to generate grids with different y^+ values. The grids can be exported as cgns-files to 2_Grids_Hexpress/<yplus>.

Grids

The folder 2_Grids_<Gridpro|Hexpress> contains the grids for the simulation. When the control file will not be adjusted, the topology and geo-files from cgns2refresco has to be called grid_<grid> and need to be in the folder 2_Grids_<Gridpro|Hexpress>/<yplus>/<grid>/refresco.

Calculations

The folder 3_Calculations_<Gridpro|Hexpress> contains the files to start the calculation and the files which will be created by ReFRESCO. To start a calculation, the job-file can be submitted to the cluster.

Postprocessing

The folder 3_Calculations_<Gridpro|Hexpress> contains several Python scripts to substract the results from the simulation files. The script getsim.py will return useful information about the simulation, for example the C_F and C_P. It can be called from the commandline:

```
python getsim.py -p <path> -y <yplus> -g <grid> -t <type>
```

Where <path> is the path to the calculation folder and <type> is either the g for Gridpro or h for Hexpress. The main script for postprocessing is postprocess.py, which will call the getsim.py function several times for all the values of y^+ and all the gridsizes. It can be called from the commandline:

```
python postprocess.py -t <type> -p <plot>
```

Where <plot> is either y (show the plots) or n (hide the plots). This script will also create a datafile in 5_Results_<Gridpro|Hexpress>/data called simdata.dat, which contains values returned by getsim.py, like C_F, C_P and the amount of cells. To do an uncertainty analysis on the grid results, the script postprocess_uncertainty.py can be called from the commandline:

```
python postprocess_uncertainty.py -t <type> -p <plot> -s <save>
```

Where <save> is either y (save the data to 6_Report/data) or n (do not save the data). This script calls the uncf.py script, which contains the uncertainty analysis proposed by Eça [32]. This script will also create a new datafile in 5_Results_<Gridpro|Hexpress>/data called simdata_p.dat with even more information than simdata.dat, like the uncertainty values and the deviation to the solution without wall functions. It also creates a lot of tex-files, which can be used to plot the data in a LaTeX report. The solution which will be taken to calculate the deviation from can be set with the script setns.py, which can be called from the commandline:

```
python setns.py -y <yplus> -g <grid> -t <type>
```

The values will be saved to nsv.dat and will be read by the postprocess_uncertainty.py script. At last, the compareresults.py script can be used to compare different grids with eachother, for example to compare Gridpro grids with Hexpress grids. It can be called from the commandline as:

```
python compareresults.py -t1 <type1> -g1 <grid1> -t2 <type2> -g2 <grid2>
```